International Journal of Earth Sciences (2022) 111:1885–1908
https://doi.org/10.1007/s00531-022-02204-2

ORIGINAL PAPER

New CA-ID-TIMS U–Pb zircon ages for the Altenberg–Teplice Volcanic Complex (ATVC) document discrete and coeval pulses of Variscan magmatic activity in the Eastern Erzgebirge (Eastern Variscan Belt)

M. Tichomirowa[1] · A. Käßner[1] · A. Repstock[2] · S. Weber[2] · A. Gerdes[3] · M. Whitehouse[4]

Received: 17 January 2022 / Accepted: 21 May 2022 / Published online: 18 June 2022

Abstract

The Altenberg–Teplice Volcanic Complex (ATVC) is a large ~ NNW–SSE trending volcano-plutonic system in the southern part of the Eastern Erzgebirge (northern Bohemian Massif, south-eastern Germany and northern Czech Republic). This study presents high precision U–Pb CA-ID-TIMS zircon ages for the pre-caldera volcano-sedimentary Schönfeld–Altenberg Complex and various rocks of the caldera stage: the Teplice rhyolite, the microgranite ring dyke, and the Sayda-Berggießhübel dyke swarm. These data revealed a prolonged time gap of ca. 7–8 Myr between the pre-caldera stage (Schönfeld–Altenberg Complex) and the climactic caldera stage. The volcanic rocks of the Schönfeld–Altenberg Complex represent the earliest volcanic activity in the Erzgebirge and central Europe at ca. 322 Ma. The subsequent Teplice rhyolite was formed during a relatively short time interval of only 1–2 Myr (314–313 Ma). During the same time interval (314–313 Ma), the microgranite ring dyke intruded at the rim of the caldera structure. In addition, one dyke of the Sayda-Berggiesshübel dyke swarm was dated at ca. 314 Ma, while another yielded a younger age (ca. 311 Ma). These data confirm the close genetic and temporal relationship of the Teplice rhyolite, the microgranite ring dyke, and (at least part of) the Sayda-Berggießhübel dyke swarm. Remarkably, the caldera formation in the south of the Eastern Erzgebirge (caldera stage of ATVC: 314–313 Ma) and that in the north (Tharandt Forest caldera: 314–312 Ma) occurred during the same time. These data document a large ~ 60 km NNW–SSE trending magmatic system in the whole Eastern Erzgebirge. For the first time, Hf-O-isotope zircon data was acquired on the ring dyke from the ATVC rocks to better characterize its possible sources. The homogeneous Hf-O-isotope zircon data from the microgranite ring dyke require preceding homogenization of basement rocks. Some small-scale melts that were produced during Variscan amphibolite-facies metamorphism show similar Hf-O-isotope characteristics and can therefore be considered as the most probable source for the microgranite ring dyke melt. In addition, a second source with low oxygen isotope ratios (e.g. basic rocks) probably contributed to the melt and possibly triggered the climactic eruption of the Teplice rhyolite as well as the crystal-rich intrusion of the ring dyke.

Keywords CA-ID-TIMS zircon dating · Erzgebirge · Variscan belt · Altenberg–Teplice Volcanic Complex · Carboniferous volcanism · Upper crustal magmatic system

Introduction

At the end of Variscan orogeny, widespread magmatic activity occurred in many regions of the Bohemian Massif (Tischendorf 1989; Förster and Romer 2010; Breiter 2012; von Seckendorff 2012; Lützner et al. 2021). In the Erzgebirge/ Krušne Hory this magmatism is often related with large ore-bearing deposits (e.g. Breiter et al. 1999). There is still considerable debate about the magmatic ages and the tempo of intrusions although more and more age data became available over the last decade. CA-ID-TIMS zircon dating is especially suitable to establish the sequence and

✉ M. Tichomirowa
tichomir@mineral.tu-freiberg.de

[1] Institut für Mineralogie, TU Bergakademie Freiberg, Brennhausgasse 14, 09599 Freiberg, Sachsen, Germany

[2] Department of Geology, Saxon State Office for Environment, Agriculture, and Geology, Halsbrücker Straße 31a, 09599 Freiberg, Germany

[3] Institut für Geowissenschaften, Goethe Universität Frankfurt, Altenhoeferallee 1, 60438 Frankfurt am Main, Germany

[4] Swedish Museum of Natural History, Box 50007, 1045 Stockholm, Sweden

periodic patterns of the Variscan magmatic activity because of its high precision (ca. ± 0.1% for individual zircon analyses and up to ± 0.03% for weighted mean sample ages; e.g. Schaltegger et al. 2015). For instance, CA-ID-TIMS zircon ages revealed multiple discrete phases of the Variscan magmatism in the Western Erzgebirge (Tichomirowa et al. 2019a). According to these data, the oldest granites (Aue-Schwarzenberg) intruded at ~ 323–322 Ma followed 2–4 Myr later by the granites of Bergen and Kirchberg. The highly evolved ore-bearing granites from the Eibenstock pluton intruded after a time lag of ~ 5 Myr at ~ 315–314 Ma. Breitkreuz et al. (2021) performed the first high precision CA-ID-TIMS data for granites and volcanics from the northern part of the Eastern Erzgebirge. Accordingly, the Niederbobritzsch granite (NBG) intruded approximately at the same time as the granites from Bergen and Kirchberg (320–318 Ma) while the volcanics from the Tharandt Forest caldera (TFC) were formed several Myr later (314–312 Ma), i.e. roughly coeval or slightly later than the Eibenstock granite in the Western Erzgebirge. However, the temporal relationship with other magmatic rocks in the Eastern Erzgebirge is still uncertain. The NBG-TFC magmatic system is located only about 10 km north of the ATVC and its temporal relationship to the ATVC still has to be determined.

Large occurrences of Variscan volcanics are absent in the Western Erzgebirge but widespread in the Eastern Erzgebirge (in addition to granites). The ATVC is interpreted to be the oldest volcanic occurrence of the late- to post-collisional Variscan magmatism in the Saxothuringian Zone of the Bohemian Massif (e.g. Hoffmann et al. 2013). It represents a giant collapse caldera. Recent publications suggest different lifetimes for this magmatic system, e.g. from ca. 324 to 300 Ma (Hoffmann et al. 2013; Casas-García et al. 2019; Tomek et al., 2022). According to Casas-García et al. (2019), the Teplice rhyolite was formed within a period between 325 and 317 Ma (the oldest dated Teichweg member yielded 323 ± 2 Ma while the youngest Cinovec member was dated 312 ± 4 Ma). Opluštil et al. (2016) dated the rhyolitic Třtěno ignimbrite by U–Pb CA-ID-TIMS on zircons at 313.41 ± 0.07 Ma. This pyroclastic density current is considered an extra-caldera equivalent of the Teplice rhyolite (Tomek et al. 2022). The Sayda–Berggießhübel dyke swarm (SBDS) was interpreted as a possible feeding system for caldera-related ignimbrites (Winter et al. 2008) and suspected to be older than the caldera collapse (Tomek et al. 2019). However, Schust (1980) and Wetzel (1984) proposed that the SBDS consists of three generations of pre-, syn- and post-caldera dykes. The microgranite ring dyke was considered as a cumulate-like magma from which the Teplice rhyolite was extracted. After the collapse of the caldera this magma intruded into feeder domains along the rims of the caldera (Müller and Seltmann 2002; Tomek et al. 2019, 2022). Therefore, it is crucial to understand the temporal relationship between the SBDS, the Teplice rhyolite, and the microgranite ring dyke.

In this study, we used high-precision zircon U–Pb CA-ID-TIMS dating to determine the ages of (i) the Teplice rhyolite (caldera stage) and the lifespan of the upper crustal Teplice magma body, (ii) the Sayda–Berggießhübel dyke swarm (SBDS), (iii) the microgranite ring dyke, and (iv) the pre-caldera stage (Schönfeld-Altenberg Complex). These data will allow us to better understand the sequence of magmatic activity in the Eastern Erzgebirge in time and space. It is also important for correlations with tuffs in Central Bohemian intramontane Permo-Carboniferous basins interpreted as outflows of the Teplice rhyolite, which are used as chronostratigraphic markers for the evolution of these sedimentary basins (Tomek et al. 2022). In addition, Hf- and O-isotope composition of zircons from the microgranite ring dyke is used to discuss possible source rocks for these magmas.

Geological setting

The Erzgebirge/ Krušné hory is part of the Variscan orogenic belt and is located at the northern margin of the Bohemian Massif (Fig. 1). It forms a NE–SW orientated crystalline complex along the German–Czech border (Fig. 1b). Petrological studies distinguished several units with different P–T histories (e.g. Rötzler et al. 1998; Schmädicke et al. 1995; Willner et al. 1997), which together represent a tectonic stack of different crustal segments formed during the Variscan subduction and continent–continent collision (e.g. Schulmann et al. 2009, 2014; Kroner and Görz 2010). Some of the eclogite- and granulite-facies rocks were buried to ultrahigh pressure (UHP) conditions at mantle depth (evidence from coesite and diamond: e.g. Schmädicke 1991; Massonne 2003). The ages suggested for peak (U)HP metamorphism cover a range from 360 to 330 Ma (e.g. Schmädicke et al. 1995, 2018; Kröner and Willner 1998; Tichomirowa et al. 2005; Tichomirowa and Köhler 2013). Gneisses form the core while mica schists and phyllites are located at the northern and western rim of the Erzgebirge.

In a late stage of the Variscan orogeny (Late Carboniferous–Early Permian) mainly acidic magmatism affected the entire Erzgebirge region. This led to the emplacement of voluminous granites (Förster et al. 1999), dyke swarms like the SBDS, and to extended volcanic systems like the ATVC and TFC in the Eastern Erzgebirge (Tischendorf 1989).

In the Eastern Erzgebirge, the magmatic activity is mainly confined along a NNW-SSE trending zone (Figs. 1b, 2). The volcanic activity is accompanied by formation of plutonic rocks. From south to north, the ATVC (Breiter et al. 2001; Hoffmann et al. 2013; Walther et al. 2016; Casas-García et al. 2019; Tomek et al. 2019, 2022), the NE-SW-trending

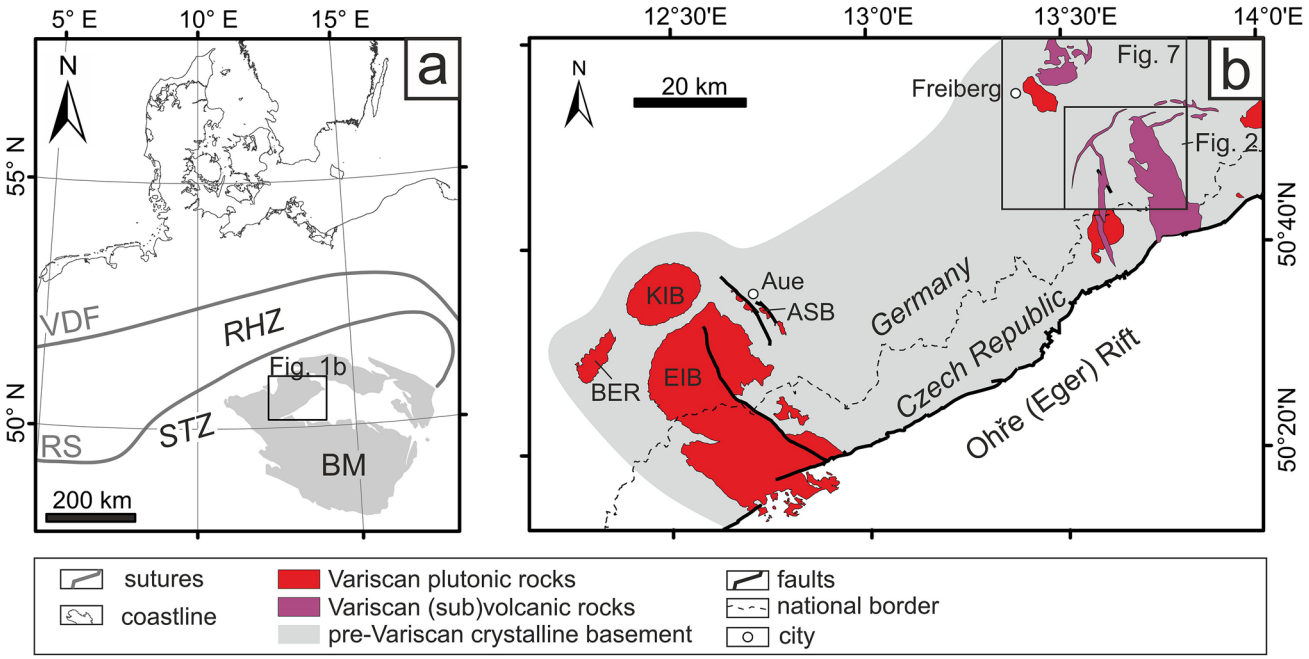

Fig. 1 **a** Simplified map showing the location of the Bohemian Massif (BM). *RS* Rheic Suture, *VDF* Variscan Deformation Front, *RHZ* Rhenohercynian Zone, *STZ* Saxothuringian Zone. **b** Simplified geological map of the Erzgebirge with various plutonic and volcanic Variscan complexes, and locations of Fig. 2 and Fig. 7. *ASB* granites from Aue-Schwarzenberg, *BER* granites from Bergen, *EIB* granites from Eibenstock/ Nejdek, *KIB* granites from Kirchberg

SBDS (Wetzel 1984; Winter et al. 2008) and the TFC-NBG (Breitkreuz et al. 2021) represent the main magmatic bodies.

The ATVC is an elongated ~ NNW–SSE trending volcano-plutonic complex (Fig. 2). About two-thirds of the ~ 36 × 18 km large trap-door caldera is exposed at the present-day erosional level (e.g. Moesta 1928; Breiter et al. 2001; Tomek et al. 2022). The ATVC hosts pre- and post-caldera plutons and a thick sequence of volcanic rocks. The ATVC rocks were grouped into three evolutionary stages (Casas-García et al. 2019). (i) The S-type biotite monzogranites of the Fláje Massif were formed as pre-collapse intrusions (Štemprok et al. 2003; Breiter 2012). They were followed by sedimentary rocks, (trachy-)dacitic pyroclastics and related subvolcanic bodies, and rhyolitic volcaniclastic successions called the Schönfeld-Altenberg Complex (SAC, Walther et al. 2016). (ii) The caldera formation is strongly related to the SBDS, the Teplice rhyolite, and microgranite ring dykes. Consequently, these rocks can be roughly assigned to the caldera stage (in a broad sense). Around the ATVC and towards the north, more than 350 dykes constitute the ~ ENE–WSW to ~ NE–SW and ~ NNW–SSE to ~ N–S-striking rhyolite dyke swarm (SBDS; Fig. 2a). The dykes reach lengths from a few metres up to several tens of kilometres, and widths from decimetres to several hundred metres (Winter et al. 2008). They do not continue into the interior of the caldera and are thus often interpreted as preceding the climactic stage (except for the intra-caldera N-S striking dykes; Mlčoch and Skácelová 2010; Tomek et al. 2019). The crystalline basement of the caldera was reached in several boreholes and dips at ca. 20–40° towards east (Moesta 1928; Benek 1991; Mlčoch and Skácelová 2010). The intra-caldera Teplice rhyolite (TR) body in the eastern part of the ATVC represents the most extensive outcrop of volcanic rocks (Fig. 2). The largest subsidence of the TR occurred in the southeastern part (Mlčoch and Skácelová 2010). The maximal thickness of TR was determined in a borehole near the city Teplice with 1033 m (Mlčoch and Skácelová 2010). Based on detailed field mapping, lithofacies analyses, stratigraphy, and whole rock geochemistry, the TR can be divided into nine lithostratigraphic units that represent three main explosive phases (e.g. Breiter et al. 2001; Casas-García et al. 2019, 2021; Tomek et al. 2022). Intercalated volcaniclastic-siliciclastic horizons document quiet periods between these eruptive phases (Fig. 2b). The TR occurs mainly as crystal-poor to crystal-rich rhyolitic ignimbrites but includes some rhyolitic and rhyodacitic lavas as well as rhyolite fallout tuffs (e.g. Lobin 1986; Breiter et al. 2001; Casas-García et al. 2019). The rapakivi-textured porphyritic microgranites are considered as contemporary intrusions forming the caldera ring dyke (Müller and Seltmann 2002; Tomek et al. 2018; "microgranite ring dyke" in Fig. 2a). (iii) The A-type granites represent the post-tectonic collapse magmatism (Breiter 2012). These are highly evolved, F-rich, albite, Li-mica, post-caldera granites of Schellerhau, Krupka, Sadisdorf, Altenberg, and Zinnwald/

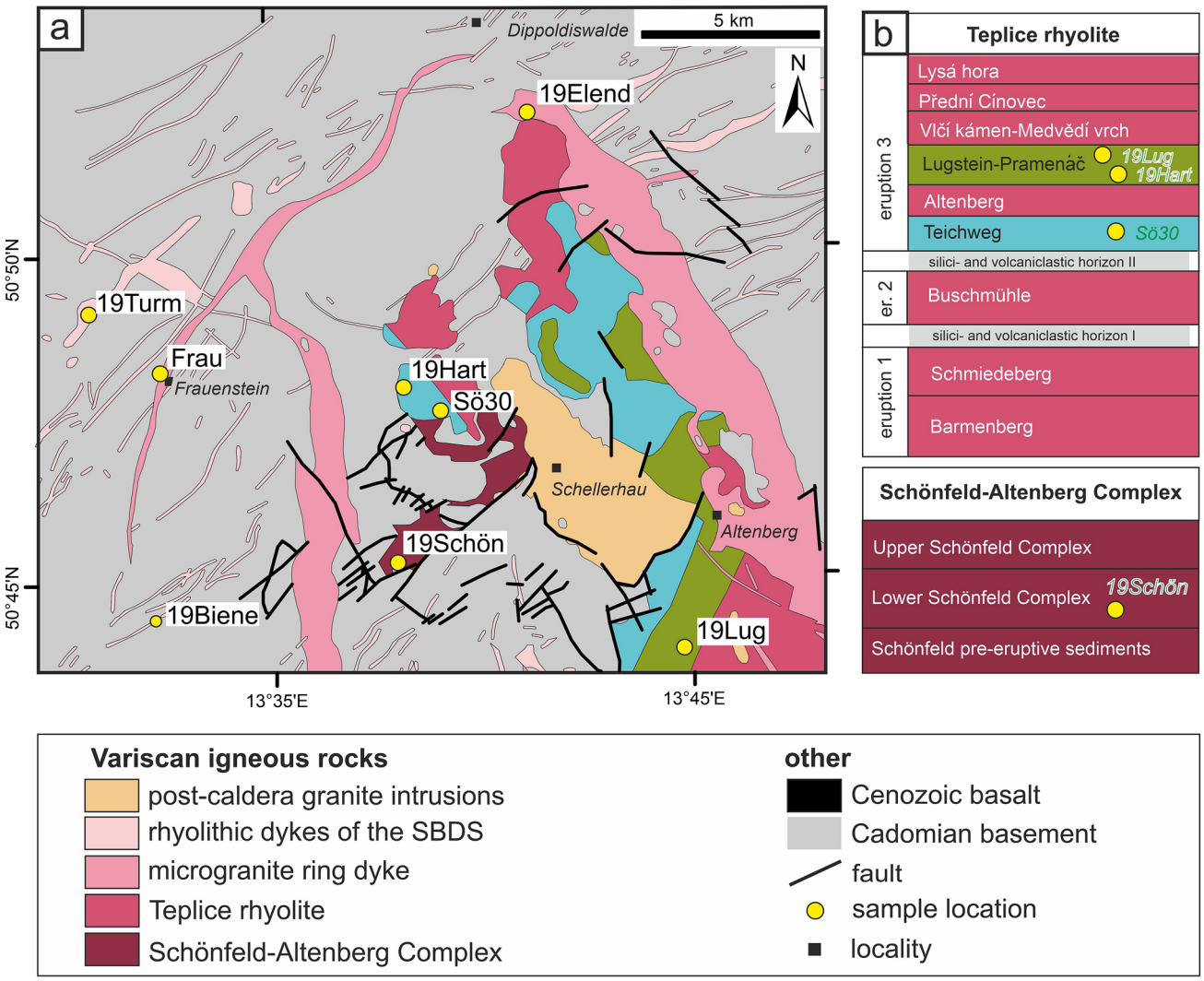

Fig. 2 **a** Simplified geological map of the southern part of the Eastern Erzgebirge with various Variscan igneous rocks (based on Hoth et al. 1995 and Sebastian 2013), and sample locations. **b** Lithostratigraphic units of the SAC and the Teplice rhyolite based on Tomek et al. (2022). The distribution of sampled members of the Teplice rhyolite (Teichweg, Lugstein-Pramenáč) is distinguished in the map based on Casas-García et al. (2021) by blue and green colours, respectively

Cínovec (Romer et al. 2007; Štemprok 2016) which often contain Sn–W greisen cupolas due to mineralization.

The ATVC erupted ca. 320 km^3 dense rock equivalent of intra-caldera volcanic facies (Casas-García et al. 2019) and at least 30 km^3 DRE of extra-caldera ignimbrites and fallout tuffs (Tomek et al. 2022). Therefore, it represents a moderately sized caldera with moderate volumes of volcanics.

Previous geochemistry and discussion on source rocks

A lot of bulk rock geochemical data exists for ATVC rocks (e.g. Breiter et al. 2001, 2012; Müller and Seltmann 2002; Štemprok et al. 2003; Breiter 2012; Walther et al. 2016; Casas-García et al. 2019, 2021). Breiter (2012) distinguished two types of magmas: (i) strongly peraluminous P-rich (S-type) magmas that mainly form the early pre-caldera stage plutons (Fláje and Niederbobritzsch granites) but also the SAC, and (ii) slightly peraluminous P-poor magmas (A-type) that form the Teplice rhyolite and the porphyritic dykes. Consequently, the later second magma type is strongly correlated with volcanic activity. Breiter (2012) interpreted that these two magma types resulted from mixing of different source rocks (quartzo-feldspathic rocks and metapelites), variations of their P–T conditions, and their water contents. According to melt inclusion studies the ATVC magma accumulated in the middle crust (Thomas 1992; Müller et al. 2006).

Various authors suggested mixing of different magmas based on variations of bulk rock chemistry and their mineral chemistry as well as core-rim structures of feldspar phenocrysts and quartz (e.g. Müller and Seltmann 2002; Müller et al. 2005; Breiter 2012). Although some authors proposed mixing of crustal magmas with a more basic melt (e.g. Müller et al. 2008; Seifert 2008), most authors exclude mixing with basic mantle-derived melts because of the exceptional scarcity of basic rocks in the Erzgebirge, the generally low contents of Mg, V, Ni, Co Cr in these igneous rocks, and the absence of mafic microgranular enclaves in the ATVC rocks (e.g. Breiter et al. 2012; Casas-García et al. 2021). Consequently, partial melting of quartzo-feldspathic metagreywacke, gneiss, metapelite, and intermediate igneous rocks have been proposed as the main source for the ATVC magmas (e.g. Breiter 2012; Breiter et al. 2012; Casas-García et al. 2021). The Cadomian basement of the Erzgebirge consists mainly of Late Neoproterozoic to Early Cambrian igneous and sedimentary rocks and Lower Paleozoic volcano-sedimentary successions. Most authors agree with the suggestion of Förster and Romer (2010) that an intensely layered, heterogeneous crustal pile with abundant fertile (qtz-fsp) lithologies (gneisses, greywackes), metapelites and subordinate mantle-derived intermediate to basic rocks that form the Cadomian basement can be considered as the most probable source rocks of Variscan igneous melts. This suggestion is based mainly on the Sr-, Nd-, and Pb-isotope compositions of these Variscan magmatic and pre-Variscan basement rocks (Förster and Romer 2010).

Samples and methods

Samples

We present the results from 8 samples from the ATVC. Table 1 lists the sample names and localities. Figure 2 shows their locations and lithostratigraphic positions. From the pre-caldera stage, we analysed one sample (19Schön; from the Schönfeld ignimbrite). Three further samples were analysed from the Teplice rhyolite (Sö30, 19Hart, 19Lug). Sample Sö30 is part of the Teichweg member, and samples 19Hart and 19Lug represent the Lugstein-Pramenáč member of the TR (Fig. 2). From the microgranite ring dyke two samples were analysed (19Elend, Frau). Finally, for the SBDS, we analysed two samples (19Biene, 19Turm).

Zircon separation

Zircons have been extracted from all eight samples by the usual procedure (crushing, Wilfley table, Frantz magnetic separator, heavy liquids, final handpicking). Selected zircons were characterized using secondary electron (SE) and cathodoluminescence (CL) images.

In general, we separated 150–200 grains from each sample, except from sample 19Turm, where we could find only 60 small grains (even after a second attempt of zircon separation). Then, for each sample ca. 30–50 zircon grains with the most idiomorphic forms (with sharp edges and even surfaces) were chosen from these overall zircon populations for further zircon dating. This was done to exclude xenocrystic zircons from further dating since the CA-ID-TIMS method is very time consuming and therefore we tried to avoid dating inherited zircons. The selected idiomorphic zircon grains usually show magmatic oscillatory zoning as shown in Fig. 3 and in the inset of Fig. 4 for sample Frau.

U–Pb Zircon dating by SHRIMP

Zircons from one sample (Frau) were analysed by the SHRIMP II technique (Sensitive High mass Resolution Ion MicroProbe) at the Centre of Isotopic Research (VSEGEI, St. Petersburg, Russia). Each analysis consisted of five scans through the mass range. The spot diameter was about 18 µm, and the primary beam intensity was about 4 nA. The data have been reduced like those used by Williams (1998,

Table 1 Sample list

Sample name	Locality	Rock type	Longitude (WGS84; decimal) N	Latitude (WGS84; decimal) E
19Schön	Quarry Hermsdorf	Schönfeld ignimbrite, LSC according to Walther et al. 2016)	50.75567	13.63081
Sö30	Drilling 2055–85, ca. 42 m depth	ATVC, Teplice ignimbrite, Teichweg member	50.79281	13.65233
19Hart	Harter Stein near Schönfeld	ATVC, Teplice ignimbrite, Lugstein-Pramenáč	50.79923	13.63545
19Lug	Kleiner Lugstein	ATVC, Teplice ignimbrite, Lugstein-Pramenáč	50.73146	13.74778
19Elend	quarry Ulberndorf	microgranite ring dyke	50.86816	13.68768
Frau	castle Frauenstein	microgranite ring dyke	50.80392	13.53869
19Biene	Bienenmühle	Sayda-Berggießhübel dyke swarm, 3. phase	50.73985	13.53567
19Turm	Turmberg	Sayda-Berggießhübel dyke swarm	50.81830	13.51018

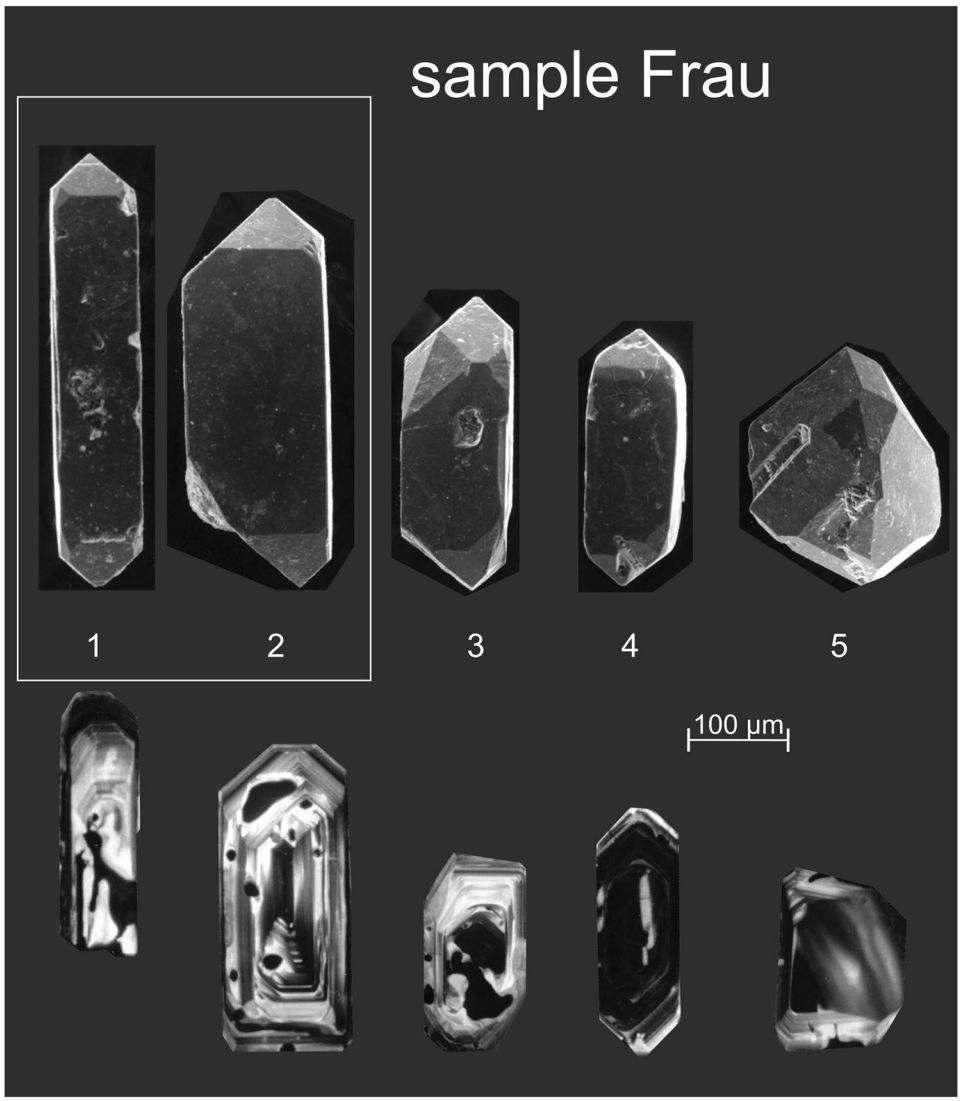

Fig. 3 Zircon SEM- (upper row) and CL-images (lower row) for selected zircon grains from sample Frau. Note that the same grains are shown in the upper and lower row. For dating with CA-ID-TIMS the most idiomorphic grains were chosen (outlined grains 1 and 2) to avoid dating of xenocrystic zircons

and references therein), using the SQUID Excel Macro of Ludwig (2000). The zircon standard Temora 2 was used for reference of the U/Pb ratio and concentrations (Black et al. 2003). Corrections for common lead (Pb_c) were made using measured ^{204}Pb and by applying the Pb evolution model of Stacey and Kramers (1975). Uncertainties given for individual analyses (ratios and ages) are at the 1σ level, for calculated Concordia ages at the 2σ level.

To trace the accuracy of any dating method, secondary reference materials should be dated together with the unknowns (Horstwood et al. 2016). Our SHRIMP data were acquired in 2011. This is the reason why a secondary standard was not analysed by the SHRIMP method.

Zircon dating by CA-ID-TIMS

Selected zircon grains (ca. 30–50 per sample) were annealed for 96 h at 900 °C, and subsequently chemically abraded for 12 h at 210 °C with concentrated HF and HNO_3 in a pressurized Parr dissolution vessel. This procedure dissolves crystal domains with strong radiation damage which are suspected to have experienced post-crystallization lead loss (Mattinson 2005). Afterwards, the acid together with dissolved zircon material was completely pipetted out and 3.5 N HNO_3 was added to the remaining zircons fragments and left for 30 min at 50 °C to remove surface lead. Several cleaning cycles with water combined with repeated ultrasonic treatment were conducted before single zircon fragments were selected for further processing. Single zircon fragments were washed with 3.5 N HNO_3 and transferred into cleaned microcapsules with a small drop of this fluid and four drops of concentrated HF. Samples were spiked with a ^{205}Pb-^{233}U-^{235}U- tracer solution (ET535 at TU Bergakademie Freiberg, Condon et al. 2015). For final dissolution, the microcapsules were placed in pressurized Parr dissolution vessels and heated

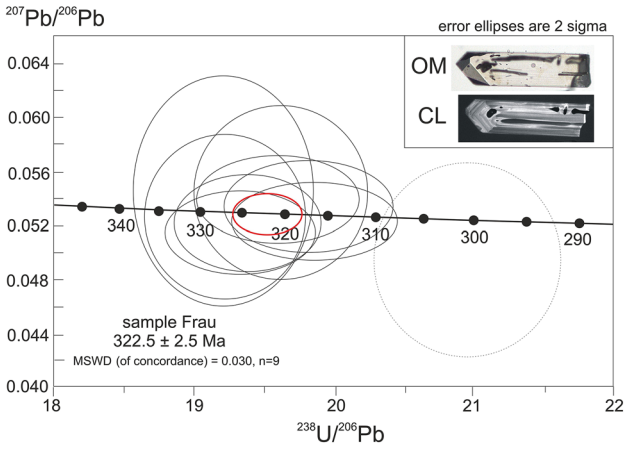

Fig. 4 SHRIMP analyses for sample Frau in a Concordia (Tera-Wasserburg) diagram. Each analysis is represented by an ellipse with its 2σ analytical uncertainty. The dotted ellipse is considered as an outlier and is not included in the Concordia age calculation. The Concordia age is shown as a red ellipse with 2σ uncertainty (including decay constant uncertainty); MSWD is given for equivalence and concordance. One selected zircon grain from this sample is shown to illustrate the idiomorphic form and internal zonation: *OM* optical microscopy, *CL* cathodoluminescence

to 200 °C for 48 h, followed by drying at 130 °C and then re-dissolution in 6 N HCl for 24 h at 200 °C to transfer them into chlorides. After repeated drying, the samples were dissolved in ten drops of 3.1 N HNO_3 and transferred into micro-columns for column chemistry. U and Pb were separated from the rest of the sample by anion exchange chromatography using HCl and H_2O. The U and Pb containing fraction was loaded on pre-degassed rhenium filaments with a drop of silica gel (Gerstenberger and Haase 1997) and measured with a Finnigan Mass Spectrometer MAT 262 using a secondary electron multiplier (SEM). Alternatively, the samples were measured on an IsotopX Phoenix Mass Spectrometer using a SEM Daly ion counter. The comparability of the results of both machines´ was proven by repeated measurement of zircon standards 91500 (Wiedenbeck et al. 1995) and Temora 2 (Black et al. 2004). The published ages of Temora 2 were determined as 416.8 ± 0.3 Ma (Black et al. 2003). Our date of 417.3 ± 0.6 Ma (data in Table 3 and Figures in Käßner et al. 2021) perfectly matches these values. Additionally, the accuracy of zircon U–Pb CA-ID-TIMS ages was monitored by dating the standard 91500. This standard was determined to be 1062.4 ± 0.4 Ma (Wiedenbeck et al. 1995) or 1063.6 ± 0.3 Ma (Schoene et al. 2006). Our weighted mean $^{206}Pb/^{238}U$-age of 1064.6 ± 1.3 Ma (data in Table 3 and Figures in Käßner et al. 2021) is within 0.1% of the accepted values. Based on the results of standard dating, we presume the here presented CA-ID-TIMS ages to be accurate on the 0.1% level.

Zircon geochemistry: Hf- and O- isotopes

For sample Frau, in addition to in situ U–Pb zircon ages analysed by SHRIMP, the Hf- and O-isotope composition was determined from the same spots of these zircon grains. Hafnium isotopes were measured on a Thermo-Finnigan Neptune multi-collector ICP-MS coupled to a Resonetics 193 nm ArF excimer laser (CompexPro 102, Coherent) system at Goethe-University Frankfurt (GUF) (Gerdes and Zeh 2006). Spots of 40–60 µm in diameter were ablated with a repetition rate of 5.5 Hz and an energy density of 5 J/cm^2 during 55 s of data acquisition. All data were adjusted relative to the JMC475 standard ($^{176}Hf/^{177}Hf = 0.282160$; Vervoort and Blichert-Toft, 1999) and quoted uncertainties are quadratic additions of the within-run precision of each analysis and the reproducibility of JMC475 (2 SD = 0.0028%, $n = 6$). We verified the accuracy and external reproducibility by repeated analysis of the reference zircons, Temora and GJ-1. They yielded $^{176}Hf/^{177}Hf$ ratios of 0.282689 ± 0.000023 (2 SD, $n = 11$ for Temora), 0.282012 ± 0.000014 (2 SD, $n = 8$ for GJ-1). This is in perfect agreement with previously published results (e.g., Gerdes and Zeh 2006; Sláma et al. 2008) and with the LA-MC-ICP-MS long-term average (2006–2012) of GJ-1 (0.282010 ± 0.000025; $n > 800$) reference zircon at GUF.

Zircon oxygen isotopes were measured with the Cameca IMS 1280 multicollector ion microprobe at the Swedish Museum of Natural History (Heinonen et al. 2015), utilizing a ~ 2 nA Cs^+ primary ion beam together with a normal incidence low-energy electron gun for charge compensation, medium field magnification (~ 80x), and two Faraday detectors (channels L2 and H2) at a typical mass resolution of ~ 2500. Measurements were performed in pre-programmed chain analysis mode with automatic field aperture and entrance slit, centered on the ^{16}O signal. The magnetic field was locked using NMR regulation for the entire analytical session. Each data acquisition run comprised a 20 × 20 µm pre-sputter to remove the Au layer, followed by the centering steps, and 64 s of data integration performed using a non-raster, ~ 10 × 10 µm spot. In the measurement chain, every set of four unknowns was followed by two bracketing analyses on the 91500 standard zircon. A $\delta^{18}O$ value of + 9.86 ‰ (SMOW, Wiedenbeck et al. 2004) was assumed for the 91500 zircon in data normalization, and small linear-drift corrections were applied to each session. The external reproducibility of ± 0.3 ‰ (1 SD) based on measurements on the standards was propagated into the overall uncertainty for each analysis.

Results

Zircon ages

Zircon U–Pb age determinations by SHRIMP

The results of sample Frau are given in Table 2 and shown in a Concordia diagram (Fig. 4). The single measurements range from 301 ± 3 to 327 ± 4 Ma but except for the youngest age (301 Ma), all other dates gave a narrow range between 317 and 327 Ma (Table 2). A Concordia age of 322.5 ± 2.5 Ma (MSWD of concordance = 0.03) was calculated from nine spot analyses excluding the measurement with the youngest age (301 Ma, Fig. 4).

Zircon U–Pb age determinations by CA-ID-TIMS

Zircon U–Pb CA-ID-TIMS isotopic results for all eight samples are presented in Table 3 and shown as $^{206}Pb/^{238}U$ ranked age plots in Fig. 5. For each sample, 8 to 21 grains were analysed by this method. Mean sample ages representing the crystallization were calculated from established age clusters with the software ET Redux (Bowring et al. 2011). The error includes the internal 2σ measurement error, the tracer calibration uncertainty, and the uncertainty of the decay constant (z error according to Schoene et al. 2006).

From sample 19Schön (Schönfeld ignimbrite) 15 zircon fragments (left after the pre-treatment with chemical abrasion) were dated (Fig. 5a). Four single grain ages are distinctly older and interpreted as xenocrystic zircons (ca. 519–518 Ma, ca. 412 Ma, ca. 338 Ma). The remaining 11 single ages vary from 312.6 Ma to 325.0 Ma. Four measurements (analyses 1, 5, 9, mp3) form a cluster with identical ages between 321.6 and 322.6 Ma. These four measurements were used to calculate a weighted mean age of 322.1 ± 0.4 Ma (MSWD = 2.6). Although one measurement (analysis 12) overlaps with this age cluster we did not include it because of its large measurement error. Five further measurements gave younger ages (between 312.6 and 320.0 Ma) that we consider as Pb loss that was not completely erased by the CA-pretreatment. Widmann et al. (2019) and Tichomirowa et al. (2019a) have shown that the "standard" leaching time of 12 h is for many samples too short to completely remove Pb loss. The remaining slight Pb loss often results in a tail towards younger ages and can explain these five younger measurements. Analysis mp2 (ca. 325 Ma) is distinctly older than the calculated age cluster and dated an antecrystic zircon (zircons incorporated during intrusion from slightly older magma batches according to Miller et al. 2007). We consider the

Table 2 Results of SHRIMP U–Pb analyses on 10 spots for sample Frau

Spot	$\frac{^{204}Pb}{^{206}Pb}$	± %	% $^{206}Pb_c$	ppm U	ppm Th	ppm $^{206}Pb^*$	$\frac{^{232}Th}{^{238}U}$	(1)$\frac{^{206}Pb}{^{238}U}$Age	(1)$\frac{^{207}Pb}{^{206}Pb}$Age	% Discordant	(1)$\frac{^{238}U}{^{206}Pb^*}$	± %	(1)$\frac{^{207}Pb^*}{^{206}Pb^*}$	± %	(1)$\frac{^{207}Pb^*}{^{235}U}$	± %	(1)$\frac{^{206}Pb^*}{^{238}U}$	± %	err corr
FRAU_1.1	0.00040	45	0.73	240	149	9.89	0.64	301.4	3.5	166	± 137	− 84	20.89	1.2	0.0494	5.9	0.326	6.0	0.04786	1.2	0.2
FRAU_4.1	0.00000	100	0.00	225	104	9.75	0.48	316.8	3.8	300	± 51	− 6	19.85	1.2	0.0523	2.2	0.363	2.6	0.05037	1.2	0.5
FRAU_3.1	0.00000	100	0.00	161	101	6.96	0.65	317.4	3.8	348	± 59	+ 9	19.82	1.2	0.0535	2.6	0.372	2.9	0.05046	1.2	0.4
FRAU_7.1	–	100	–	131	92	5.73	0.73	320.6	4.0	385	± 110	+ 17	19.61	1.3	0.0543	4.9	0.382	5.1	0.05100	1.3	0.3
FRAU_5.1	–	—	–	188	128	8.24	0.70	321.1	3.8	363	± 55	+ 12	19.58	1.2	0.0538	2.4	0.379	2.7	0.05107	1.2	0.4
FRAU_6.1	–	–	–	297	168	13.1	0.58	322.2	3.5	360	± 44	+ 11	19.51	1.1	0.0537	2.0	0.380	2.3	0.05125	1.1	0.5
FRAU_9.1	0.00006	100	0.11	321	136	14.2	0.44	324.4	3.5	288	± 65	− 13	19.37	1.1	0.0521	2.8	0.370	3.0	0.05161	1.1	0.4
FRAU_2.1	0.00000	100	0.00	297	210	13.2	0.73	325.3	3.6	259	± 57	− 26	19.32	1.1	0.0514	2.5	0.367	2.7	0.05175	1.1	0.4
FRAU_10.1	0.00021	71	0.38	179	119	7.98	0.69	327.0	3.8	308	± 110	− 6	19.22	1.2	0.0525	4.8	0.377	5.0	0.05203	1.2	0.2
FRAU_8.1	0.00020	100	0.36	97	59	4.35	0.63	327.2	4.4	400	± 140	+ 19	19.20	1.4	0.0547	6.3	0.393	6.4	0.05207	1.4	0.2

Errors are 1-sigma; Pb_c and Pb^* indicate the common and radiogenic portions, respectively

Error in TEMORA Standard calibration was 0.25%

(1) Common Pb corrected using measured ^{204}Pb

Table 3 U–Pb CA-ID-TIMS single-grain zircon dates and isotopic data

Fraction	Dates (Ma)								Composition			Isotopic ratios						
	$^{206}Pb/^{238}U$	±2σ	$^{207}Pb/^{235}U$	±2σ	$^{207}Pb/^{206}Pb$	±2σ	Corr	% disc	Pb*	Pb_c	Pb*/Pb_c	$^{206}Pb/^{204}Pb$	$^{206}Pb/^{238}U$	±2σ	$^{207}Pb/^{235}U$	±2σ	$^{207}Pb/^{206}Pb$	±2σ
	a	(abs.)	a	(abs.)	a	(abs.)	coef	b	(pg) c	(pg) d	e	f	g	(%)	g	(%)	g	(%)
Schönfeld ignimbrite																		
19Schön																		
19Schoen-1	321.9	0.3	324.7	1.4	344.9	11.2	0.187	6.7	135.2	3.3	40.6	2206.61	0.05120	0.09	0.37686	0.50	0.0534	0.49
19Schoen-2	519.2	0.6	525.3	5.1	551.8	26.9	0.088	5.9	32.0	2.6	12.1	842.85	0.08388	0.11	0.67758	1.24	0.0586	1.23
19Schoen-3	312.7	0.4	313.8	4.9	322.3	41.11	0.059	3.0	38.2	3.6	10.5	638.85	0.04970	0.13	0.36215	1.81	0.0529	1.81
19Schoen-4	312.6	0.4	314.8	4.5	331.3	37.3	0.072	5.7	37.5	3.4	11.2	702.89	0.04969	0.12	0.36350	1.65	0.0531	1.64
19Schoen-5	321.8	0.7	322.9	10.7	330.9	87.52	0.023	2.8	19.3	4.1	4.7	311.71	0.05119	0.23	0.37444	3.86	0.0531	3.86
19Schoen-6	411.6	1.0	418.4	14.2	456.1	91.9	0.015	9.8	18.7	4.9	3.8	276.84	0.06592	0.26	0.50988	4.14	0.0561	4.14
19Schoen-7	517.8	0.9	513.9	11.4	496.4	62.1	0.028	− 4.3	35.0	6.4	5.5	391.46	0.08364	0.18	0.65876	2.82	0.0572	2.82
19Schoen-8	318.3	0.6	318.0	7.2	315.3	59.8	0.016	− 1.0	39.4	6.2	6.4	450.09	0.05062	0.18	0.36771	2.63	0.0527	2.63
19Schoen-9	322.6	0.4	323.7	6.0	332.1	48.8	0.035	2.9	31.6	3.8	8.3	543.15	0.05131	0.14	0.37552	2.15	0.0531	2.15
19Schoen-10	320.0	0.9	314.6	14.3	274.9	120.7	0.023	− 16.4	23.2	7.2	3.2	238.40	0.05088	0.29	0.36315	5.27	0.0518	5.27
19Schoen-11	338.0	5.4	332.0	88.8	289.8	716.9	0.006	− 16.7	3.1	4.9	0.6	55.46	0.05384	1.65	0.38674	31.34	0.0521	31.38
19Schoen-12	320.7	6.4	309.9	107.3	229.9	929.0	0.006	− 39.5	4.4	9.0	0.5	48.13	0.05101	2.06	0.35697	40.18	0.0508	40.22
19Schoenmp-1	317.1	0.3	317.8	2.6	323.6	21.5	0.111	2.0	70.0	3.8	18.4	1210.10	0.05041	0.10	0.36755	0.95	0.0529	0.95
19Schoenmp-2	325.0	0.9	319.4	13.8	279.2	115.2	0.025	− 16.4	30.6	7.2	4.3	247.23	0.05171	0.29	0.36972	5.03	0.0519	5.03
19Schoenmp-3	321.6	1.4	311.1	22.6	233.2	194.5	0.038	− 37.9	26.1	10.1	2.6	158.38	0.05115	0.46	0.35849	8.43	0.0508	8.43
Teplice ignimbrite																		
Sö30																		
So30_1	318.5	1.5	322.1	24.6	348.0	201.3	0.019	8.5	8.1	3.8	2.2	145.59	0.05065	0.50	0.37327	8.90	0.05345	8.90
So30_2	312.3	0.8	315.6	12.7	340.0	106.5	0.018	8.1	15.1	3.7	4.1	258.25	0.04964	0.26	0.36453	4.70	0.05326	4.70
So30_3	309.0	0.3	311.0	3.6	325.8	30.1	0.073	5.2	48.9	3.3	14.6	880.05	0.04911	0.09	0.35839	1.33	0.05293	1.33
So30_4	299.7	0.4	305.4	4.9	349.3	42.2	0.045	14.2	53.5	5.1	10.6	620.63	0.04759	0.13	0.35094	1.87	0.05348	1.86
So30_5	315.4	0.2	316.5	1.3	323.9	11.0	0.204	2.6	132.9	3.5	38.2	2393.91	0.05015	0.06	0.36570	0.50	0.05289	0.49
So30_6	312.7	0.4	315.2	5.8	333.8	48.9	0.032	6.3	35.7	3.9	9.2	541.07	0.04970	0.14	0.36397	2.16	0.05312	2.16
So30_7	313.8	0.6	317.6	6.9	345.8	57.0	0.071	9.2	28.0	3.5	8.1	457.87	0.04988	0.18	0.36726	2.53	0.05340	2.52
So30_8	340.7	6.5	343.9	106.6	365.5	824.8	0.002	6.8	43.4	78.1	0.6	49.20	0.05427	1.97	0.40305	36.54	0.05387	36.59
So30b-1	311.5	0.4	312.9	5.4	323.0	45.5	0.030	3.6	85.2	8.4	10.1	586.12	0.04951	0.12	0.36088	2.00	0.05289	2.00
So30b-2	314.5	0.5	314.8	6.2	317.0	52.0	0.040	0.8	32.6	3.8	8.5	515.70	0.04999	0.15	0.36343	2.29	0.05275	2.29
So30b-3	313.3	0.2	315.0	3.1	328.1	26.1	0.065	4.5	56.3	3.3	16.9	999.68	0.04979	0.08	0.36376	1.15	0.05301	1.15
So30b-4	314.1	0.3	316.5	3.6	334.4	29.6	0.042	6.1	52.0	3.3	15.7	881.64	0.04992	0.10	0.36573	1.31	0.05316	1.31
So30b-5	313.2	0.2	312.9	1.6	310.7	13.5	0.154	− 0.8	121.4	3.7	32.7	1916.05	0.04978	0.08	0.36092	0.60	0.05260	0.59
So30b-6	313.9	0.4	316.1	6.6	332.2	55.1	0.029	5.5	27.8	3.3	8.4	483.45	0.04990	0.15	0.36518	2.43	0.05310	2.43
So30b-7	315.8	0.3	315.4	3.6	312.2	30.3	0.051	− 1.2	46.2	3.1	15.0	872.63	0.05021	0.09	0.36423	1.33	0.05264	1.33
So30b-8	306.4	0.6	248.2	5.4	− 271.8	60.0	0.504	212.7	51.8	6.1	8.5	542.96	0.04867	0.21	0.27686	2.46	0.04127	2.36
So30b-9	314.1	0.3	312.1	3.1	296.7	26.5	0.038	− 5.9	30.3	1.8	17.0	973.64	0.04994	0.09	0.35982	1.16	0.05228	1.16

Table 3 (continued)

Fraction	Dates (Ma)								Composition			Isotopic ratios						
	$^{206}Pb/^{238}U$	±2σ	$^{207}Pb/^{235}U$	±2σ	$^{207}Pb/^{206}Pb$	±2σ	Corr	% disc	Pb*	Pb_c	Pb*/Pb_c	$^{206}Pb/^{204}Pb$	$^{206}Pb/^{238}U$	±2σ	$^{207}Pb/^{235}U$	±2σ	$^{207}Pb/^{206}Pb$	±2σ
	a	(abs.)	a	(abs.)	a	(abs.)	coef	b	(pg) c	(pg) d	e	f	g	(%)	g	(%)	g	(%)
So30c-1	314.5	0.5	314.4	5.5	313.4	45.8	0.064	− 0.3	35.1	3.5	10.0	583.81	0.05000	0.18	0.36289	2.02	0.05267	2.01
So30c-2	313.5	0.4	316.6	5.2	339.3	43.0	0.031	7.6	40.2	3.5	11.3	612.48	0.04984	0.13	0.36588	1.90	0.05327	1.90
So30c-3	314.3	0.4	316.4	3.7	332.1	30.6	0.054	5.4	22.0	1.4	15.5	851.78	0.04997	0.12	0.36568	1.35	0.05310	1.35
So30c-4	313.0	0.4	316.0	4.7	338.0	39.4	0.046	7.4	40.4	3.5	11.4	666.28	0.04976	0.12	0.36508	1.74	0.05324	1.74
19Hart																		
19Hart-1	311.5	0.3	315.3	1.5	343.1	12.0	0.169	9.2	101.1	2.9	34.6	2133.10	0.04951	0.09	0.36413	0.54	0.05336	0.53
19Hart-2	307.0	0.5	312.4	0.8	352.9	5.3	0.575	13.0	202.6	2.8	71.2	4427.05	0.04878	0.15	0.36029	0.29	0.05359	0.23
19Hart-3	309.4	0.3	312.3	2.2	334.5	18.9	0.065	7.5	77.0	3.4	23.0	1374.83	0.04916	0.09	0.36016	0.83	0.05316	0.83
19Hart-4	312.9	0.3	316.2	2.8	340.5	23.2	0.092	8.1	39.5	2.2	18.1	1110.14	0.04973	0.09	0.36533	1.03	0.05330	1.02
19Hartb-1	606.8	0.7	996.8	3.9	1994.9	10.8	0.139	69.6	63.8	4.6	13.9	823.63	0.09871	0.12	1.66906	0.61	0.12269	0.61
19Hartb-2	313.2	0.4	315.7	2.5	333.9	21.2	0.091	6.2	64.9	3.2	20.0	1226.00	0.04979	0.12	0.36464	0.94	0.05314	0.93
19Hartb-3	313.9	0.5	316.6	5.4	335.9	44.7	0.070	6.5	31.6	3.3	9.6	588.03	0.04991	0.16	0.36584	1.98	0.05319	1.97
19Hartb-4	314.4	0.5	318.2	4.8	346.4	40.0	0.073	9.2	37.7	3.6	10.6	652.02	0.04998	0.15	0.36805	1.77	0.05344	1.77
19Hartb-5	313.6	0.4	314.7	3.0	322.9	24.9	0.119	2.9	57.2	3.4	16.7	1044.84	0.04986	0.13	0.36339	1.10	0.05289	1.09
19Hartb-6	314.1	0.4	316.1	2.6	331.2	21.6	0.148	5.2	68.4	3.5	19.4	1195.88	0.04993	0.14	0.36524	0.96	0.05308	0.95
19Hartb-7	315.1	0.5	316.4	5.8	326.2	48.0	0.052	3.4	31.3	3.6	8.7	553.50	0.05009	0.17	0.36561	2.12	0.05296	2.11
19Hartb-8	314.0	0.4	316.0	4.6	330.7	38.2	0.091	5.1	42.7	3.8	11.2	685.05	0.04992	0.14	0.36507	1.69	0.05307	1.68
19Hartb-9	314.3	0.5	315.8	6.4	326.7	53.0	0.069	3.8	42.9	5.4	8.0	501.64	0.04997	0.18	0.36483	2.34	0.05297	2.33
19Lug																		
19Lug-1	307.8	0.4	311.3	4.6	337.5	39.2	0.059	8.8	112.8	10.6	10.7	670.83	0.04891	0.12	0.35876	1.73	0.05323	1.73
19Lug-2	313.4	0.4	316.0	3.7	335.6	30.9	0.081	6.6	49.4	3.6	13.6	843.22	0.04982	0.14	0.36514	1.37	0.05318	1.36
19Lug-3	312.5	0.5	315.4	6.5	336.3	54.0	0.042	7.1	32.7	4.2	7.8	491.51	0.04968	0.16	0.36423	2.38	0.05320	2.38
19Lug-4	314.2	0.4	317.2	3.6	339.7	29.5	0.079	7.5	38.6	2.8	14.0	879.73	0.04994	0.12	0.36671	1.31	0.05328	1.30
19Lug-5	311.6	0.3	314.2	3.2	334.0	26.6	0.085	6.7	69.1	4.5	15.4	976.14	0.04952	0.11	0.36269	1.18	0.05315	1.17
19Lug-6	312.0	0.4	314.3	4.6	331.5	38.4	0.070	5.9	48.6	4.5	10.9	683.35	0.04959	0.13	0.36282	1.70	0.05309	1.69
19Lug-7	310.8	0.4	314.2	2.8	339.1	22.9	0.113	8.3	53.4	3.0	18.0	1122.42	0.04940	0.12	0.36264	1.02	0.05327	1.01
19Lug-8	311.7	0.4	313.3	5.1	325.0	42.8	0.050	4.1	42.0	4.2	10.0	618.66	0.04954	0.13	0.36142	1.89	0.05294	1.89
19Lug-9	307.6	0.7	311.3	10.3	339.3	86.7	0.023	9.4	24.3	4.9	4.9	313.18	0.04887	0.23	0.35877	3.83	0.05327	3.83
19Lugb-1	314.8	1.4	317.7	22.6	338.9	187.83	0.014	7.1	8.0	3.4	2.3	154.58	0.05005	0.46	0.36739	8.29	0.05326	8.29
19Lugb-2	329.1	0.6	348.5	7.9	479.5	59.0	0.026	31.3	23.0	3.6	6.4	414.81	0.05238	0.18	0.40945	2.67	0.05671	2.67
19Lugb-3	311.5	0.5	314.2	6.7	334.7	56.2	0.033	6.9	35.8	4.8	7.5	474.20	0.04950	0.16	0.36268	2.48	0.05316	2.48
19Lugb-4	312.1	0.5	313.6	7.2	324.8	60.3	0.024	3.9	34.4	4.8	7.2	445.13	0.04960	0.16	0.36182	2.65	0.05293	2.66
19Lugb-5	314.2	0.7	315.9	9.8	328.6	82.1	0.026	4.4	17.1	3.1	5.5	331.67	0.04994	0.21	0.36491	3.62	0.05300	3.62
19Lugb-6	316.2	2.4	311.6	39.1	277.1	333.9	0.016	− 14.1	4.7	3.6	1.3	98.13	0.05027	0.78	0.35911	14.57	0.05181	14.58
19Lugb-7	314.4	0.8	318.5	11.8	348.6	97.6	0.026	9.8	13.4	3.2	4.2	278.50	0.04999	0.26	0.36848	4.31	0.05347	4.32
19Lugb-8	314.4	1.6	317.8	24.9	342.9	206.5	0.011	8.3	13.4	6.6	2.0	142.16	0.04999	0.51	0.36756	9.12	0.05333	9.12

Table 3 (continued)

Fraction	Dates (Ma)								Composition			Isotopic ratios						
	$^{206}Pb/^{238}U$	±2σ	$^{207}Pb/^{235}U$	±2σ	$^{207}Pb/^{206}Pb$	±2σ	Corr	% disc	Pb*	Pb_c	Pb*/Pb_c	$^{206}Pb/^{204}Pb$	$^{206}Pb/^{238}U$	±2σ	$^{207}Pb/^{235}U$	±2σ	$^{207}Pb/^{206}Pb$	±2σ
	a	(abs.)	a	(abs.)	a	(abs.)	coef	b	(pg) c	(pg) d	e	f	g	(%)	g	(%)	g	(%)
Porphyritic microgranite																		
19Elend																		
19Elend-1	313.2	0.7	314.8	1.8	326.6	14.6	0.321	4.1	101.0	3.5	28.9	1770.92	0.04978	0.23	0.36345	0.68	0.05297	0.64
19Elend-2	312.5	1.2	314.8	2.5	331.7	19.2	0.424	5.8	68.0	3.1	21.8	1336.75	0.04967	0.40	0.36340	0.94	0.05309	0.85
19Elend-3	312.4	0.4	315.3	3.0	337.0	25.7	− 0.113	7.3	49.3	3.1	16.0	1005.59	0.04965	0.11	0.36416	1.12	0.05322	1.13
19Elend-4	313.2	1.3	312.6	3.5	308.4	27.4	0.341	− 1.6	44.0	2.8	15.7	949.58	0.04979	0.43	0.36058	1.28	0.05255	1.20
19Elend-5	313.6	0.6	315.5	6.1	329.4	51.0	0.078	4.8	25.3	3.0	8.5	520.72	0.04985	0.21	0.36436	2.26	0.05304	2.25
19Elend-6	311.4	0.8	314.2	1.9	334.6	14.5	0.381	6.9	64.0	2.2	28.7	1759.56	0.04949	0.26	0.36260	0.69	0.05316	0.64
19Elend-7	312.4	0.4	316.0	4.4	343.3	36.5	0.062	9.0	34.8	3.0	11.7	714.77	0.04965	0.12	0.36515	1.62	0.05336	1.61
19Elend-8	311.1	0.3	314.9	3.9	342.9	32.6	0.064	9.3	44.4	3.4	13.0	798.73	0.04944	0.11	0.36357	1.44	0.05335	1.44
19Elend-9	311.5	0.3	315.4	3.1	344.4	26.0	0.093	9.5	51.9	3.3	16.0	991.37	0.04951	0.11	0.36432	1.15	0.05339	1.15
19Elend-10	310.5	0.4	313.3	5.5	334.7	46.3	0.056	7.2	36.7	4.0	9.2	569.71	0.04934	0.14	0.36151	2.05	0.05316	2.04
19Elend-11	312.8	0.6	315.2	9.5	332.9	79.9	0.025	6.0	25.5	4.7	5.5	339.46	0.04973	0.20	0.36403	3.52	0.05312	3.52
Frau																		
Frau1-1	315.2	0.4	315.7	6.1	319.7	51.1	0.025	1.4	27.7	3.2	8.6	522.80	0.05011	0.13	0.36470	2.25	0.05281	2.25
Frau1-2	314.3	0.5	313.8	7.0	310.4	59.3	0.019	− 1.3	26.1	3.5	7.4	456.56	0.04996	0.15	0.36215	2.60	0.05260	2.60
Frau1-3	314.2	0.7	318.1	9.9	346.5	82.3	0.027	9.3	21.4	4.1	5.2	326.22	0.04995	0.23	0.36792	3.64	0.05344	3.64
Frau1-4	313.3	0.4	315.0	3.1	327.5	26.2	0.098	4.3	25.8	1.6	15.9	957.60	0.04981	0.15	0.36377	1.16	0.05299	1.15
Frau1-5	313.0	0.2	313.8	2.1	319.6	17.5	0.107	2.1	82.0	3.4	24.2	1487.36	0.04976	0.07	0.36214	0.78	0.05281	0.77
Frau1-6	313.7	0.3	314.4	5.1	319.0	43.0	0.027	1.6	34.7	3.4	10.2	619.10	0.04987	0.11	0.36287	1.89	0.05279	1.89
Frau1-7	312.2	0.7	313.7	11.0	325.0	92.7	0.005	3.9	19.2	4.2	4.6	294.82	0.04962	0.24	0.36202	4.08	0.05293	4.08
Frau1-8	314.3	0.6	315.7	9.6	325.6	80.7	0.025	3.5	19.0	3.5	5.4	337.41	0.04997	0.20	0.36466	3.55	0.05295	3.55
Frau1-9	314.2	0.4	314.3	6.1	315.0	51.0	0.026	0.3	27.4	3.2	8.6	526.01	0.04995	0.13	0.36285	2.24	0.05270	2.24
Sayda-Berggießhübel Dyke Swarm (SBDS)																		
19Biene																		
19Biene-1	306.9	0.2	309.7	1.3	330.9	10.5	0.244	7.3	148.6	3.8	38.6	2397.37	0.04876	0.08	0.35664	0.47	0.05307	0.46
19Biene-2	307.7	0.9	309.5	14.8	322.9	126.4	0.013	4.7	33.9	10.0	3.4	222.77	0.04889	0.31	0.35638	5.56	0.05289	5.57
19Biene-3	307.4	0.4	308.4	3.6	315.7	30.5	0.100	2.6	71.6	5.1	13.9	862.19	0.04884	0.14	0.35485	1.35	0.05272	1.34
19Biene-4	309.1	0.4	310.1	2.6	317.3	22.0	0.100	2.6	58.9	3.0	19.4	1170.27	0.04912	0.12	0.35715	0.97	0.05276	0.97
19Bieneb-1	304.7	0.3	296.2	2.6	229.3	23.4	0.098	− 32.9	90.7	5.0	18.3	1178.76	0.04841	0.09	0.33870	1.02	0.05077	1.01
19Bieneb-2	305.8	0.3	306.7	3.9	313.5	33.3	0.062	2.5	59.1	4.6	13.0	797.48	0.04858	0.11	0.35263	1.47	0.05267	1.46
19Bieneb-3	306.4	0.3	306.8	2.2	310.1	18.7	0.117	1.2	76.3	3.4	22.5	1393.98	0.04868	0.09	0.35280	0.83	0.05259	0.82
19Bienebk-1	310.8	0.5	311.3	6.6	315.0	56.3	0.047	1.3	24.9	3.3	7.5	477.72	0.04940	0.18	0.35878	2.48	0.05270	2.47
19Bienebk-2	311.0	0.4	312.3	5.4	321.8	45.4	0.030	3.4	27.7	3.1	9.0	585.38	0.04943	0.14	0.36008	2.00	0.05286	2.00
19Bienebk-3	310.7	1.1	313.2	17.7	332.0	149.0	0.013	6.4	10.0	3.4	2.9	190.65	0.04938	0.37	0.36132	6.57	0.05310	6.57

Table 3 (continued)

Fraction	Dates (Ma)								Composition			Isotopic ratios						
	$^{206}Pb/^{238}U$	±2σ	$^{207}Pb/^{235}U$	±2σ	$^{207}Pb/^{206}Pb$	±2σ	Corr	% disc	Pb*	Pb_c	Pb*/Pb_c	$^{206}Pb/^{204}Pb$	$^{206}Pb/^{238}U$	±2σ	$^{207}Pb/^{235}U$	±2σ	$^{207}Pb/^{206}Pb$	±2σ
	a	(abs.)	a	(abs.)	a	(abs.)	coef	b	(pg) c	(pg) d	e	f	g	(%)	g	(%)	g	(%)
19Bienecg-1	310.6	0.6	313.0	8.9	330.7	74.9	0.060	6.1	17.0	2.9	5.8	358.94	0.04937	0.21	0.36105	3.31	0.05307	3.30
19Bienecg-2	308.5	0.4	310.3	4.3	323.5	36.4	0.062	4.6	41.8	3.6	11.5	725.45	0.04902	0.12	0.35740	1.60	0.05290	1.60
19Turm																		
19Turm-1	313.3	0.6	316.2	8.0	337.5	66.5	0.003	7.2	33.0	5.2	6.4	402.49	0.04979	0.20	0.36528	2.93	0.05323	2.93
19Turm-2	313.0	0.4	313.6	1.8	317.9	14.8	0.174	1.5	68.6	2.4	28.2	1685.22	0.04975	0.12	0.36184	0.66	0.05277	0.65
19Turm-3	312.7	0.4	314.9	4.3	331.2	36.0	0.069	5.6	40.5	3.4	11.9	727.16	0.04970	0.13	0.36359	1.59	0.05308	1.59
19Turm-4	312.4	0.4	315.3	1.5	336.9	12.2	0.220	7.3	118.4	3.6	33.3	2027.92	0.04966	0.12	0.36417	0.55	0.05321	0.54
19Turm-5	323.5	0.5	324.7	5.4	333.8	44.1	0.048	3.1	56.3	5.4	10.5	597.64	0.05146	0.15	0.37685	1.95	0.05314	1.95
19Turm-6	313.5	0.8	315.0	12.2	326.2	102.0	0.018	3.9	19.8	4.9	4.1	270.90	0.04983	0.26	0.36374	4.49	0.05296	4.49
19Turm-7	314.3	0.8	315.7	10.7	325.6	89.8	0.043	3.4	15.9	3.2	4.9	304.01	0.04997	0.25	0.36464	3.96	0.05295	3.95
19TurmN-1	313.9	0.4	315.9	2.0	330.5	16.8	0.141	5.0	90.8	3.6	25.5	1534.98	0.04991	0.12	0.36496	0.75	0.05304	0.74
Standard 91500																		
91500-1	1059.6	2.7	1065.5	19.1	1063.6	53.0	0.958	0.4	13.4	3.5	3.8	258.44	0.17989	0.27	1.85578	2.90	0.07482	2.63
91500-2	1060.1	2.4	1054.3	16.1	1044.8	45.0	0.899	0.3	35.8	8.0	4.5	302.03	0.17853	0.25	1.82457	2.46	0.07412	2.23
91500-3	1061.1	2.0	1056.3	4.0	1047.0	10.5	0.582	1.3	76.7	7.0	11.0	696.59	0.17886	0.18	1.82997	0.61	0.07420	0.52
91500-4	1061.9	1.8	1062.4	11.8	1066.9	32.8	0.884	1.3	22.1	3.6	6.2	406.34	0.17877	0.19	1.84717	1.79	0.07494	1.63
91500-5	1062.3	3.4	1060.6	23.6	1062.6	65.6	0.933	0.0	10.9	3.5	3.1	211.95	0.17866	0.35	1.84214	3.58	0.07478	3.26
91500-6	1063.0	2.1	1055.6	9.2	1042.1	25.6	0.662	2.3	77.3	9.4	8.2	537.07	0.17912	0.21	1.82811	1.40	0.07402	1.27
91500-7	1063.3	1.1	1063.8	6.9	1066.8	19.2	0.844	0.3	69.5	6.5	10.6	684.59	0.17915	0.12	1.85099	1.05	0.07494	0.95
91500-8	1063.5	1.4	1059.9	3.2	1055.9	8.6	0.656	3.3	59.6	6.1	9.7	632.30	0.17907	0.09	1.84020	0.48	0.07453	0.43
91500-9	1064.5	2.9	1059.2	3.5	1052.5	9.6	0.532	1.1	59.4	6.2	9.5	618.90	0.17918	0.15	1.83823	0.54	0.07440	0.48
91500-10	1064.6	2.9	1064.6	3.6	1072.4	9.6	0.575	4.3	55.4	7.8	7.1	463.58	0.17887	0.14	1.85328	0.54	0.07514	0.48
91500-11	1064.9	1.2	1064.9	5.2	1066.4	14.4	0.674	0.1	109	7.6	14.3	920.28	0.17948	0.13	1.85409	0.79	0.07492	0.71
91500-12	1065.3	1.2	1061.3	1.0	1055.1	1.7	0.863	5.3	278	7.7	36.2	2298.51	0.17951	0.08	1.84394	0.15	0.07450	0.09
91500-13	1065.8	2.4	1064.5	15.3	1064.1	42.2	0.866	0.2	57.2	12	4.7	318.17	0.17957	0.25	1.85287	2.31	0.07484	2.10
91500-14	1066.2	1.4	1064.9	6.4	1064.5	17.5	0.711	6.3	45.5	3.9	11.6	748.51	0.17966	0.14	1.85418	0.97	0.07485	0.87
91500-15	1067.6	2.9	1065.8	21.6	1065.0	59.8	0.969	0.2	41.4	12	3.4	230.99	0.17986	0.30	1.85672	3.27	0.07487	2.97
Standard Temora2																		
Tem-1	415.5	1.9	414.3	24.8	412.5	152.1	0.980	0.7	6.64	3.3	2.0	148.73	0.06644	0.49	0.50390	7.28	0.05501	6.80
Tem-2	416.5	1.9	416.7	3.1	419.2	17.4	0.547	0.6	185	9.9	18.6	1183.26	0.06670	0.40	0.50739	0.92	0.05517	0.78
Tem-3	416.8	0.9	418.3	11.0	429.1	66.6	0.931	2.9	15.6	3.4	4.6	301.97	0.06673	0.23	0.50984	3.20	0.05542	2.99
Tem-4	417.1	0.8	415.9	1.9	409.5	11.0	0.602	1.8	71.6	6.8	10.5	666.04	0.06683	0.10	0.50621	0.55	0.05493	0.49
Tem-5	417.2	0.6	417.9	5.9	423.4	36.1	0.865	1.5	32.8	3.8	8.7	561.55	0.06680	0.14	0.50913	1.74	0.05528	1.62
Tem-6	417.4	0.6	413.3	2.2	395.5	13.2	0.643	5.5	60.8	7.7	7.9	515.59	0.06674	0.09	0.50238	0.64	0.05459	0.59
Tem-7	417.8	0.7	414.3	2.1	401.4	12.9	0.653	4.1	62.6	11	6.0	399.61	0.06676	0.08	0.50385	0.63	0.05473	0.57
Tem-8	417.8	2.1	423.4	23.2	457.0	138.6	0.811	8.6	12.3	5.4	2.3	157.82	0.06686	0.58	0.51736	6.71	0.05612	6.25
Tem-9	418.2	0.9	418.6	6.3	422.6	38.1	0.756	1.0	31.3	5.9	5.3	350.33	0.06696	0.17	0.51016	1.83	0.05526	1.71

Table 3 (continued)

Fraction	Dates (Ma)							Composition			Isotopic ratios							
	$^{206}Pb/^{238}U$	±2σ	$^{207}Pb/^{235}U$	±2σ	$^{207}Pb/^{206}Pb$	±2σ	Corr	% disc	Pb*	Pb_c	Pb*/Pb_c	$^{206}Pb/^{204}Pb$	$^{206}Pb/^{238}U$	±2σ	$^{207}Pb/^{235}U$	±2σ	$^{207}Pb/^{206}Pb$	±2σ
	a	(abs.)	a	(abs.)	a	(abs.)	coef	b	(pg) c	(pg) d	e	f	g	(%)	g	(%)	g	(%)
Tem-10	419.3	0.6	417.8	7.9	411.6	47.9	0.960	1.9	20.0	3.1	6.5	429.87	0.06714	0.16	0.50902	2.29	0.05499	2.14
Tem-11	419.7	1.9	417.5	18.8	408.8	114.7	0.828	2.7	12.6	4.6	2.8	192.09	0.06718	0.45	0.50865	5.49	0.05492	5.13
Tem-12	425.3	0.9	422.0	11.0	406.6	66.6	0.921	4.6	15.8	3.4	4.7	317.05	0.06812	0.23	0.51526	3.19	0.05486	2.97
Tem-13	429.5	1.8	422.2	22.8	387.7	138.8	0.958	10.8	8.40	3.7	2.2	161.86	0.06874	0.45	0.51563	6.61	0.05440	6.18

[a]Isotopic dates calculated using the decay constants lambda 238 = 1.55125 E-10 and lambda 235 = 9.8485 E-10 (Jaffey et al. 1971)

[b]% discordance = 100 – (100 × ($^{206}Pb/^{238}U$ date) / ($^{207}Pb/^{206}Pb$ date))

[c]Total mass of radiogenic Pb

[d]Total mass of common Pb

[e]Ratio of radiogenic Pb (including ^{208}Pb) to common Pb

[f]Measured ratio corrected for fractionation and spike contribution only

[g]Measured ratios corrected for fractionation and tracer and blank

calculated mean age (322.1 ± 0.4 Ma) as the magmatic formation age of the Schönfeld ignimbrite.

Altogether, 21 single grain ages were determined from sample Sö30 (Fig. 5b). In the first attempt (analyses numbers 1–8 in Table 3) we applied the standard leaching time (12 h) during chemical abrasion. The single ages vary between 299.7 ± 0.4 and 318.5 ± 1.5 Ma (except for one distinctly older age at 340.7 ± 6.5 Ma). We suggested that the large age scatter towards younger ages resulted from remaining Pb loss. For this reason, we applied an additional leaching procedure (24 instead of 12 h, analysis numbers b-1 to b-9 in Table 3). The single ages from zircons leached 24 h show less scatter (from 306.4 ± 0.6 to 315.8 ± 0.3 Ma) and support our suggestion of Pb loss for the youngest single dates. However, the variation of these single ages is still too large to exclude an important impact of Pb loss and to ensure a correct mean age calculation. Therefore, we applied an additional leaching step (36 h instead of 12 h) to the remaining zircon fragments. From the 36 h leached zircons only four measurements were possible (analyses numbers c-1 to c-4) resulting in a very narrow range between 313.0 ± 0.4 to 314.5 ± 0.5 Ma again supporting the interpretation that the younger single ages are too young because of Pb loss in this sample. Six single measurements gave identical (within error) dates between 313.9 ± 0.4 and 314.5 ± 0.5 Ma (all from fractions b and c) and define a mean age of 314.2 ± 0.4 Ma.

From sample 19Hart, 13 single grain analyses were performed (Fig. 5b). From the first attempt (12 h standard leaching, numbers 1–4 in Table 3) we got variable single dates between 307.0 ± 0.5 Ma to 312.9 ± 0.3 Ma. We applied additional leaching (24 h instead of 12 h) to verify that Pb loss did not play a role for these unexpected young ages. The 24 h leached zircons (analyses numbers b-1 to b-9 in Table 3) recorded single ages between 313.2 ± 0.4 and 315.1 ± 0.5 Ma (except one xenocrystic age at ca. 607 Ma) and are thus older than all measurements from the first leaching step (12 h). Identical ages were obtained from five measurements (all from fractions b, i.e. 24 h leaching) resulting in a weighted mean age of 314.1 ± 0.4 Ma (MSWD = 0.7). One slightly older age (315.1 ± 0.5 Ma) is considered as an antecrystic zircon grain.

For sample 19Lug, 17 measurements were performed (Fig. 5b). After 12 h leaching, we got variable single ages from 307.6 ± 0.7 to 314.2 ± 0.4 Ma (analyses numbers 1–9 in Table 3). After applying additional 12 h leaching (24 h instead of 12 h) most dates vary between 311.5 ± 0.5 and 316.2 ± 2.4 Ma (except one older age at 329.1 ± 0.6 Ma considered as an antecrystic zircon grain). Six measurements yielded identical ages but we decided to exclude the measurement with the highest error (316.2 ± 2.4 Ma). The weighted mean age from the remaining five measurements results in 314.2 ± 0.5 Ma (MSWD = 0.3) considered as the

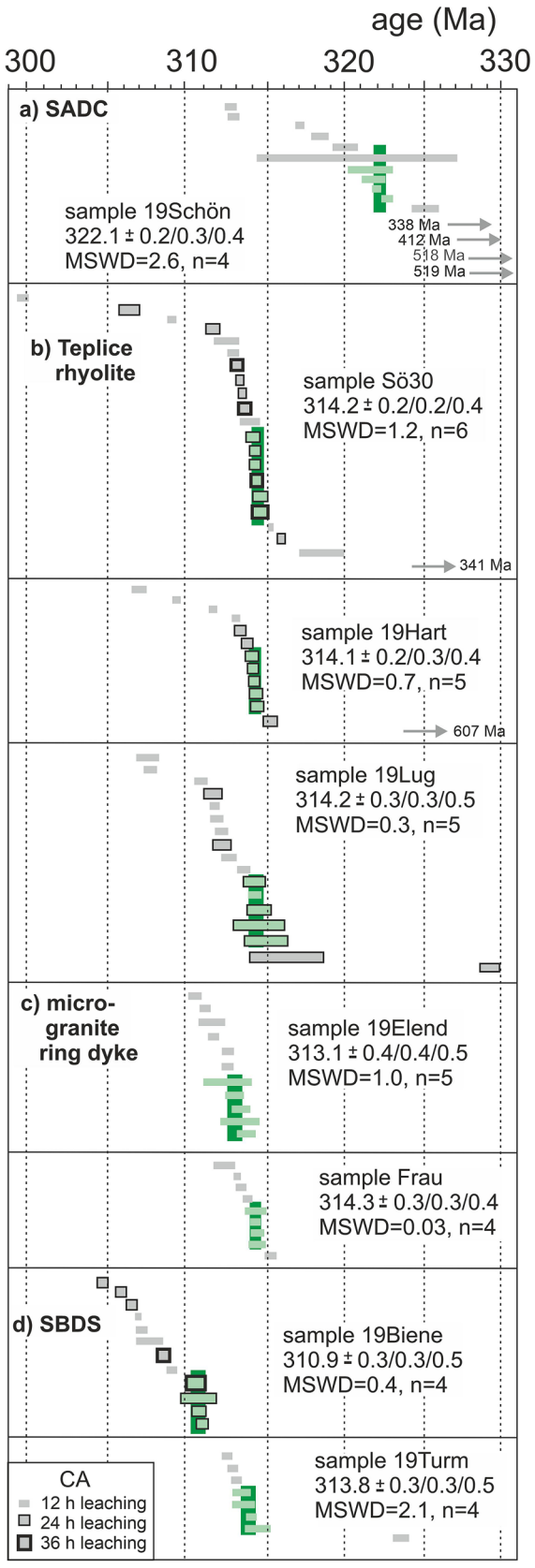

Fig. 5 Single grain zircon analyses and $^{206}Pb/^{238}U$ weighted mean ▶ dates for analysed samples. Each horizontal bar represents a single zircon grain analysis including its 2σ analytical (internal) uncertainty. Grey bars are not included in the weighted mean calculation. Green vertical bars represent the weighted mean age, with the associated 2σ uncertainty. Uncertainty of the weighted mean dates is reported as ± *x*/*y*/*z*, with *x*—as 2*σ* internal, *y*—2*σ* external uncertainty including tracer calibration and *z*—2*σ* external uncertainty including ^{238}U decay constant uncertainty; *MSWD* mean square of weighted deviates

eruption age of this sample. The ten younger ages reflect various (but small) degrees of Pb loss. Summarizing, all three samples from the Teplice rhyolite yielded identical mean ages (Sö30: 314.2 ± 0.4 Ma, 19Hart: 314.1 ± 0.4 Ma; 19Lug: 314.2 ± 0.5 Ma).

Two samples were dated from the adjacent microgranite ring dyke. All age data of sample 19Elend cluster between 310.5 ± 0.4 and 313.6 ± 0.6 Ma (Table 3: 11 analyses). The oldest five single dates yielded identical ages resulting in a mean age of 313.1 ± 0.5 Ma (MSWD = 1.0). A tail towards younger ages is considered as slight Pb loss ($n = 6$; Fig. 5c). The second sample Frau also shows a generally small variation of single ages (between 312.2 ± 0.7 and 315.2 ± 0.4 Ma; Table 3; Fig. 3c). One single slightly older age (315.2 ± 0.5 Ma) is considered as antecrystic zircon. From the remaining eight measurements the oldest four dates form a cluster with a mean age of 314.3 ± 0.4 Ma (MSWD = 0.03). The other four measurements form a tail towards younger ages implying slight Pb loss.

Two samples were dated from the SBDS. Twelve measurements were performed for sample 19Biene. After 12 h leaching, the single ages vary from 306.9 ± 0.2 Ma to 309.1 ± 0.4 Ma. These ages are significantly younger than for all other samples. A second leaching step (24 h instead of 12 h) was applied to reduce possible Pb loss. The three analyses from this data set yielded even slightly younger ages (304.7 ± 0.3 to 306.3 ± 0.3 Ma, Table 3: analyses numbers b-1 to b-3). Then, two groups of zircons were separated: small and large grains. For the small grains, 24 h of leaching was applied to ensure that the grains were not completely dissolved during this step. From the remaining parts of the zircons, only three measurements were possible yielding ages between 310.7 ± 1.1 and 311.0 ± 0.4 Ma (Table 3, analyses numbers bk-1 to bk-3). For the large grains, 36 h leaching was applied. The two measurements yielded ages of 308.5 ± 0.4 and 310.6 ± 0.6 Ma (Table 3: analyses numbers cg-1 and cg-2). The four oldest dates form a cluster with a mean age of 310.9 ± 0.5 Ma (MSWD = 0.4). All other measurements form a tail to younger ages considered as Pb loss (Fig. 5d).

In general, the zircon yield for the sample 19Turm was rather low and the zircons were small. Seven measurements yielded ages between 312.4 ± 0.4 and 314.3 ± 0.8 Ma with one significantly older age (323.5 ± 0.5 Ma) considered as

a xenocrystic zircon. From newly separated zircons from the heavy mineral fraction, only one measurement was possible (analysis number N in Table 3) yielding an age at 313.9 ± 0.4 Ma (Fig. 5d). The four oldest dates form a cluster with a mean age of 313.8 ± 0.5 Ma (MSWD = 2.1).

Zircon geochemistry: Hf- and O- isotope ratios

The zircons from sample Frau have uniform Hf and very homogeneous O isotopic compositions (Table 4). The hafnium isotope ratio $^{176}Hf/^{177}Hf$ varies from 0.282570 to 0.282610 (corresponding to $\varepsilon Hf(t) = -0.6$ to $+0.9$ (t = 320 Ma)), and the oxygen isotope value ($\delta^{18}O$) varies from 6.0 to 6.6 ‰. Hf model ages range from 1.1 to 1.2 Ga.

Discussion

Comparison of zircon ages from the same samples/locations obtained by different methods (LA-ICP-MS, SHRIMP, CA-ID-TIMS)

Dating of the same samples (or samples from the same location) with different zircon dating methods should result in identical ages. In this section, we discuss zircon ages obtained from the same sample locations while in the next section we compare our new ages with published ages from other localities of the ATVC.

Two of our samples from the Teplice rhyolite were dated before with LA-ICP-MS by Casas-García et al. (2019). Sample Sö30 was taken from borehole 2055–85 at a depth of ca. 42 m. It was dated by Casas-García et al. (2019) with 323 ± 2 Ma. The sample 19Hart (sample HS-1 in Casas-García et al. 2019) was dated with LA-ICP-MS at 313 ± 3 Ma. This age is within error identical to our new CA-ID-TIMS age (314.1 ± 0.4 Ma) while the age of sample 2055–85 [42] is ca. 9 Ma older (corresponding to a 3% shift). The latter LA-ICP-MS Concordia age was calculated from 6 single measurements out of a total of 63 LA-ICP-MS measurements (Casas-García et al. 2019: Fig. 7a). Therefore, only few selected measurements could be used for the Concordia age calculation. We suggest that this selection can be the reason for the age bias between the two different dating methods. The single zircon CA-ID-TIMS measurements of this sample (Sö30) showed the largest within sample variations due to the highest degree of Pb loss even after 12 h and 24 h leaching (Fig. 5b). Therefore, it is not easy to get an accurate zircon age for this sample without applying CA (as is the usual procedure for LA-ICP-MS dating).

Sample Frau was dated by SHRIMP (322.5 ± 2.5 Ma) and by CA-ID-TIMS (314.3 ± 0.4 Ma). These ages do not overlap and the difference is ca. 2.6% (8.2 Ma). The accuracy of our SHRIMP age cannot be assessed, because it was determined without a parallel measurement of a secondary standard in 2011. Thus, the uncertainty is only a statistical error, excluding external components. The absolute age resolution of SHRIMP has been estimated as 1–2% (Schaltegger et al. 2015).

Tichomirowa et al. (2019a) compared CA-ID-TIMS with SHRIMP and LA-ICP-MS ages from the same samples of Variscan granites from the Western Erzgebirge. While single SHRIMP ages based on ca. 10 measurements can show deviations from CA-ID-TIMS ages (from 0 to ± 3%), the mean age of several samples from the same pluton (corresponding to > 30 SHRIMP data points) resulted in a SHRIMP age identical with CA-ID-TIMS data. Therefore, we suggest that the small number of single SHRIMP data points for sample Frau (n = 9) may explain the deviation to the CA-ID-TIMS age.

Timescale of Variscan magmatic activity in the ATVC (pre-caldera and caldera stage)

Figure 6 compares our new zircon CA-ID-TIMS data with published ages. It shows that our new data are in most cases consistent with previous studies on dating, especially with recently published LA-ICP-MS ages from Tomek et al. (2019, 2022) and with most LA-ICP-MS data from Casas-García et al. (2019). In a few cases distinct ages were published as the possible too young K–Ar ages by Müller et al. (2005), one too young Ar–Ar age (Seltmann and Schilka 1995), and one too old Pb-Pb zircon age for the microgranite ring dyke (Kempe et al. 1999).

The new zircon data show that there is a significant time gap of ca. 8 Myr between the pre-caldera phase and the caldera phase. In contrast to the supposed 11 Myr duration for the Teplice rhyolite (Casas-García et al. 2019), the CA-ID-TIMS data (our data: 314.2 ± 0.4 Ma, 314.1 ± 0.4 Ma, 314.2 ± 0.5 Ma, and that of Opluštil et al. 2016: 313.4 ± 0.4 Ma) suggest a much shorter lifetime of only 1–2 Myr for various members of the Teplice rhyolite. However, it should be noted that our three samples all represent the last TR eruption stage 3 (Fig. 2) while the lithostratigraphic position of the extra-caldera equivalent of TR is unclear (Tomek et al. 2022). Similar durations (1–2 Myr) have recently been obtained by CA-ID-TIMS ages for other Variscan plutonic and volcanic suites (e.g. Tichomirowa et al. 2019a; Lützner et al. 2021; Breitkreuz et al. 2021; Käßner et al. 2021).

According to the new age data, the microgranite ring dyke (314.3 ± 0.4 Ma, 313.1 ± 0.5 Ma) was formed approximately during the same time interval as the Teplice rhyolite. These data support the idea of the coeval formation of the microgranite ring dyke with the climactic stage of the Teplice ignimbrite as was supposed earlier (Müller and Seltmann 2002; Müller et al. 2005; Tomek et al. 2019, 2022).

Table 4 LA-MC-ICPMS Lu–Hf isotope data of zircon from sample Frau

	$^{176}Yb/^{177}Hf$ (a)	±2σ	$^{176}Lu/^{177}Hf$ (a)	±2σ	$^{178}Hf/^{177}Hf$	$^{180}Hf/^{177}Hf$	Sig Hf (b) (V)	$^{176}Hf/^{177}Hf$	±2σ (c)	$^{176}Hf/^{177}Hf$(t) (d)	εHf(t) (d)	±2σ (c)	TNC (e) (Ga)	age (f) (Ma)	±2σ	$\delta^{18}O$ ‰
Frau1-1a	0.0160	13	0.00057	4	1.46711	1.88675	11.29	0.282584	21	0.282581	− 0.1	0.7	1.16	320	15	6.1
Frau1-2a	0.0290	27	0.00100	8	1.46715	1.88672	10.36	0.282598	22	0.282592	0.3	0.8	1.14	320	15	6.3
Frau2-1a	0.0247	20	0.00085	5	1.46720	1.88668	11.10	0.282597	23	0.282592	0.3	0.8	1.14	320	15	6.6
Frau2-3a	0.0228	22	0.00080	6	1.46710	1.88662	10.71	0.282615	20	0.282610	0.9	0.7	1.10	320	15	6.0
Frau3-1a	0.0242	20	0.00086	5	1.46716	1.88662	9.40	0.282606	20	0.282601	0.6	0.7	1.12	320	15	6.1
Frau3-2a	0.0133	11	0.00048	3	1.46715	1.88677	10.94	0.282570	19	0.282567	− 0.6	0.7	1.19	320	15	6.2
Frau3-3a	0.0207	18	0.00072	5	1.46719	1.88682	9.72	0.282579	27	0.282574	− 0.3	0.9	1.17	320	15	6.2
Frau3-6a	0.0196	16	0.00069	4	1.46710	1.88669	9.13	0.282586	20	0.282582	− 0.1	0.7	1.16	320	15	6.0
Frau4-8a	0.0242	20	0.00084	5	1.46712	1.88665	10.53	0.282600	20	0.282595	0.4	0.7	1.13	320	15	6.3
Frau4-9a	0.0114	9	0.00041	2	1.46716	1.88668	10.50	0.282585	16	0.282582	− 0.1	0.6	1.16	320	15	6.2
Temora ($n=14$)	0.0273	217	0.00097	65	1.46712	1.88657	8	0.282689	23	0.282682	5.6	0.8	0.92	417	3	
GJ-1 ($n=32$)	0.0073	18	0.00025	3	1.46714	1.88672	9	0.282012	14	0.282009	− 14.0	0.5	2.15	606	6	
JMC 475 ($n=6$)					1.46718	1.88669	11	0.282165	8							

Quoted uncertainties (absolute) relate to the last quoted figure. The effect of the inter-element fractionation on the Lu/Hf was estimated to be about 6% or less based on analyses of the GJ-1 and Plesoviče zircon. Accuracy and reproducibilty was checked by repeated analyses (n = 30 and 20, respectively) of reference zircon GJ-1 and Plesoviče (data given as mean with 2 standard deviation uncertainties)

(a) $^{176}Yb/^{177}Hf = (^{176}Yb/^{173}Yb)_{true} \times (^{173}Yb/^{177}Hf)_{meas} \times (M_{173(Yb)}/M_{177(Hf)})^{b(Hf)}$, $b(Hf) = \ln(^{179}Hf/^{177}Hf_{true}/^{179}Hf/^{177}Hf_{measured})/\ln(M_{179(Hf)}/M_{177(Hf)})$, M = mass of respective isotope. The $^{176}Lu/^{177}Hf$ were calculated in a similar way by using the $^{175}Lu/^{177}Hf$ and b(Yb)

(b) Mean Hf signal in volt

(c) Uncertainties are quadratic additions of the within-run precision and the daily reproducibility of the 40 ppb-JMC475 solution. Uncertainties for the JMC475 quoted at 2SD (2 standard deviation)

(d) Initial $^{176}Hf/^{177}Hf$ and eHf calculated using the apparent Pb-Pb age determined by SHRIMP dating (see column f), and the CHUR parameters: $^{176}Lu/^{177}Hf = 0.0336$, and $^{176}Hf/^{177}Hf = 0.282785$ (Bouvier et al. 2008)

(e) two stage model age in billion years using the measured $^{176}Lu/^{177}Lu$ of each spot (first stage = age of zircon), a value of 0.0113 for the average continental crust (second stage), and a juvenile crust (NC) $^{176}Lu/^{177}Lu$ and $^{176}Hf/^{177}Hf$ of 0.0384 and 0.28314, respectively

(f) apparent Pb-Pb age determined by LA-ICP-MS

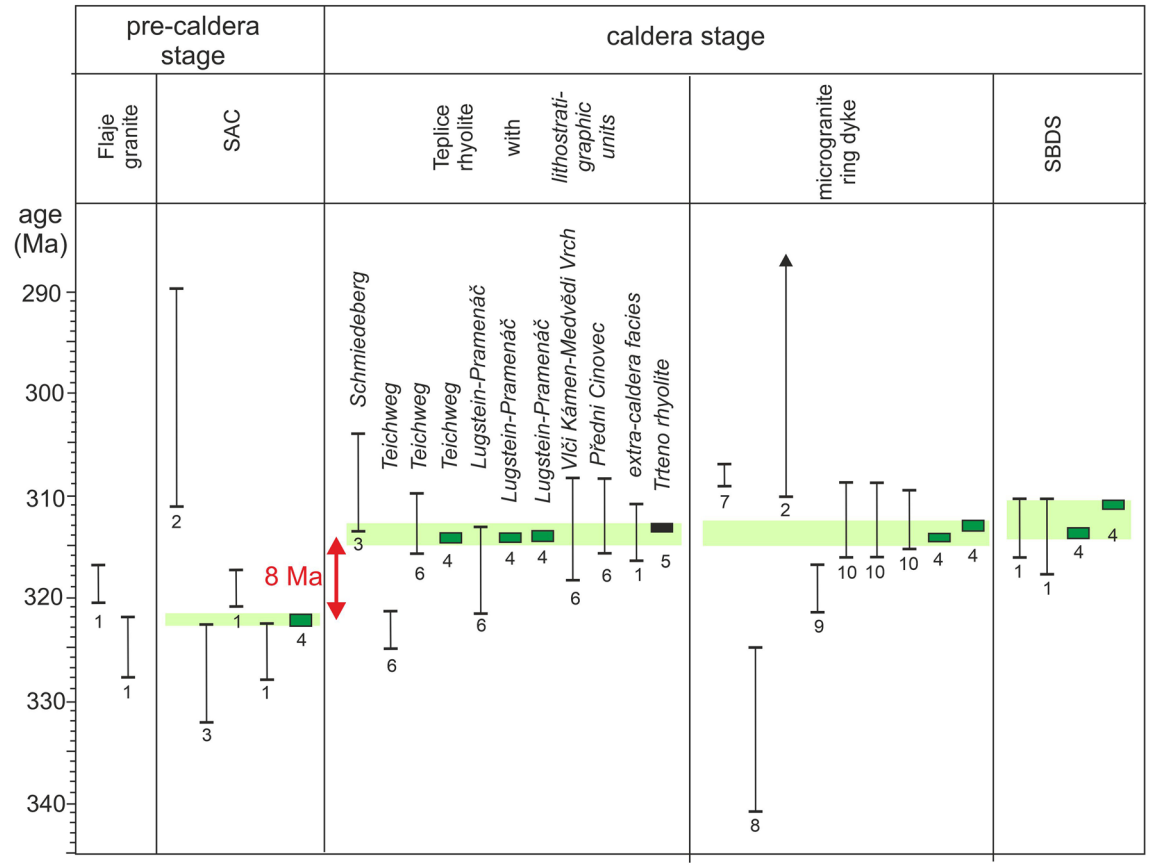

Fig. 6 Published age data for ATVC rocks compared to the ages from this study. Literature data are given with black lines/boxes (mean ages with their 2σ uncertainty), data from this study are shown with filled green boxes (mean ages with their 2σ uncertainty). Light green bars represent the total variation of CA-ID-TIMS ages for all analysed samples and are discussed in the text. Numbers give the references to the data source: 1: Tomek et al. (2022), 2: Müller et al. (2005), 3: Hoffmann et al. (2013), 4 – this study, 5: Opluštil et al. (2016), 6: Casas-García et al. (2019), 7: Seltmann and Schilka (1995), 8: Kempe et al. (1999), 9: Romer et al. (2010), 10: Tomek et al. (2019)

Accordingly, the age range obtained by high-precision dating (314–313 Ma) is the best estimate for the climactic stage of the ATVC. In addition, at least part of the SBDS intruded during the same time interval or slightly later (313.8 ± 0.5 Ma, 310.8 ± 0.5 Ma) although several authors suggest a pre-caldera age for the SBDS based on field relationships (Mlčoch and Skácelová 2010; Tomek et al. 2019).

Timescale of Variscan magmatic activity in the Eastern Erzgebirge

According to the new data, the SAC (ca. 322 Ma) is roughly contemporaneous with the Flaje granite (Tomek et al., 2022; Fig. 6) and slightly older than Niederbobritzsch granite (ca. 320–318 Ma; Breitkreuz et al. 2021). The older age of the SAC implies a higher erosion level (at or close to surface) already at 322 Ma in the southern part of the Eastern Erzgebirge (Fig. 7). The SAC age dates the first appearance of (sub)volcanic (mainly dacitic) activity in the Eastern Erzgebirge at ca. 322 Ma representing the earliest preserved post-Variscan volcano-sedimentary rocks in central Europe. However, the main volcanic activity with the largest volumes of erupted volcanic rocks took place ca. 7–8 Myr later. Two calderas formed during this stage: the ATVC-caldera in the south (mainly at 314–313 Ma) and the Tharandt Forest caldera (ca. 315–312 Ma), which is located ca. 10 km north of ATVC (Fig. 7). This implies a large and long-standing (at least from 315 to 312 Ma) upper crustal magmatic system in the whole Eastern Erzgebirge stretching about 60 km along a NNW-SSE trending zone that is parallel to the Elbe Fault Zone. Magma systems that fed voluminous eruptions—such as the Teplice eruptions of the Eastern Erzgebirge—are known for their extreme longevity (0.1 to 1 Myr up to 10 Myr, e.g. de Silva and Gregg 2014; Glazner 2021). For instance, the Altiplano-Puna Volcanic Complex in Bolivia hosts multiple supereruptions within a 10 Myrs magmatic flare-up with up to 3 Myr resting time in volcanic activity (de Silva and Gregg 2014). Both the Flaje granite and the volcanic Schönfeld formation in the south, as well as the Niederbobritzsch granite in the north (which

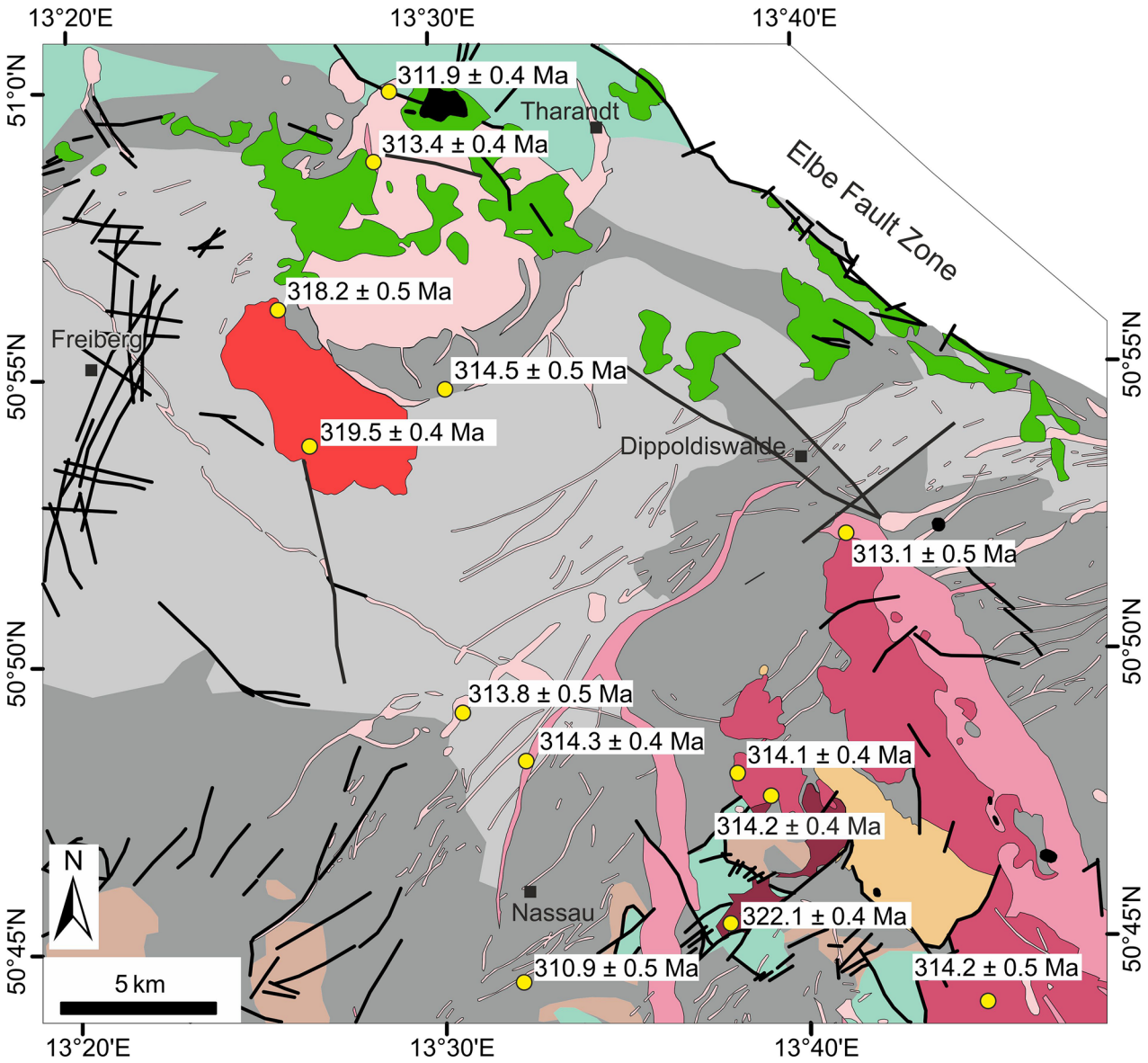

Fig. 7 Geological map of the Eastern Erzgebirge (German part) showing the spatial distribution of CA-ID-TIMS ages (Breitkreuz et al., 2021, this study) for various Variscan igneous rocks. The geological map is based on Hoth et al. (1995) and Sebastian (2013)

formed ca. 5–8 Ma earlier), could have caused a continuous increase in upper crustal temperatures and led to an elevated geotherm and produced a ductile halo in the host rocks in the pre-eruption level for the later voluminous eruptions. According to de Silva and Gregg (2014), this preheating of the upper crust is considered a major prerequisite for long-living caldera-forming magma reservoirs.

The coeval age of the ring dyke system (ca. 314–313 Ma; two samples from this study and one sample from Breitkreuz et al. 2021) supports its genetic relationship to the climactic stage. These mainly subvertical ring dykes mark the rim of the ATVC caldera structure and mainly follow two directions: (i) especially in the south they form the NNW-SSE trending rims of the ATVC, but (ii) they also occur in NE-SW directions, south from the TFC (Fig. 7). The dykes from the SBDS (ca. 314 Ma and 311 Ma) mainly follow the same two directions (Fig. 7). Consequently, these dykes probably played an important role during and slightly after the climactic stage as supposed before (e.g. Tomek et al. 2019). Therefore, they can be interpreted (i) as the former magma chamber roof (as suggested by Christiansen 2001 for the Yellowstone Volcanic supereruption), (ii) as faults propagating downwards into the magma chamber from an uplifted and extended roof (de Silva and Gregg 2014), or (iii) as post-climactic and post-collapse dykes that erupted along faults bounding the flanks of a resurgent dome (Folkes et al. 2011). Mlčoch and Skácelová (2010) interpreted the block west of the Teplice rhyolite body up to the western ring dyke (they call it "Altenberg Block") as a roof pendant. Here, mainly gneisses from the basement crop out as well as remnants of low-grade Early Paleozoic rocks (phyllites/mica schists and metabasites) that occur also in the basement of the SAC. In this "Altenberg Block" the Teplice rhyolite has been eroded due to the eastward trap-door tilt and the downsagging of the caldera floor (Benek 1991; Tomek et al. 2019). Accordingly, the ring dykes most likely represent syn-climactic dykes propagating downwards into the magma chamber in the sense of de Silva and Gregg (2014).

Remarkably, during or slightly after the climactic stage of the ATVC and TFC, intense plutonic magmatic activity took also place further to the east along the NNW-SSE trending Intra-Sudetic line as evidenced by the large Karkonosze Pluton (Kryza et al. 2014: ca. 313–312 Ma) and by smaller granitic plutons in Lusatia (Käßner et al. 2021: ca. 313–312 Ma). Together with the dominant NNW-SSE trend of the ATVC and their porphyritic ring dykes this underlines the important role of the WNW-ESE extensional stress field during this period (Edel et al. 2018).

Until now precise CA-ID-TIMS dates for the post-caldera granite magmatism of the ATVC (evolutionary stage 3 of the ATVC rocks according to Casas-García et al. 2019) are missing. The magmatic activity may have lasted until about 305 Ma (according to the age compilation done by Tomek et al. 2022; their Fig. 12), although contradictory ages still do not allow a robust time to estimate for these post-collapse igneous rocks.

Possible source rocks of Variscan magmatic rocks: what information can Hf- and O-isotopes from zircons add?

For sample Frau, Hf- and O-Isotope values were determined on the same spot locations where the SHRIMP ages were produced. This ensures that all analyses are determined from zircons formed in the Variscan melt (no xenocrystic ages). Zircon is an early crystallizing mineral in granites and very robust against late-stage (e.g. hydrothermal) overprints. In contrast to bulk rock chemistry, $^{176}Hf/^{177}Hf$ isotope ratios in zircons are not affected by fractionation processes and hence represent the melt composition (Chen and Zheng 2017). Melt production always results in increased Hf-isotope compositions in newly formed zircons compared to the source (Chen and Zheng 2017). For our samples, all Hf isotope analyses show a remarkable homogeneity in their epsilon values but also in their $\delta^{18}O$ values (Fig. 8). Bindemann and Valley (2002) have shown that homogenous $\delta^{18}O$ values are common for long-lived voluminous pyroclastic eruptions. They interpreted this large-scale $\delta^{18}O$ melt homogeneity as evidence for magma chambers longevity and convection. In turn, the convective stirring of large magma bodies requires underplating and/or recharge of magmas over long periods. From geophysical measurements (seismic measurements, Bouger gravity low, e.g. Conrad et al. 1994) as well as from many drill cores (Mlčoch and Skácelová 2010; Berger et al., 2011) it is suggested that Variscan magmatic rocks continue for several kilometers downwards in the Erzgebirge. In this context, it should be noted that granulitic and small scale amphibolitic melts were produced in the gneisses already during the Variscan metamorphism (Tichomirowa et al., 2018). Thus, the preceding Variscan metamorphism could contribute to an increase in the upper crustal geotherm in the Erzgebirge.

Although Hf-O studies on zircons from the Bohemian Massif are still limited, zircons from the microgranite ring dyke plot in a specific narrow field (Fig. 8) that has slightly higher epsilon Hf values compared to Variscan granites from the Western Erzgebirge, the Koenigshain granite from Lusatia, and to zircons with the highest values from rhyolites from the NE German basin (Fig. 8; Pietranik et al. 2013; Słodczyk et al. 2018; Tichomirowa et al. 2018, 2019b; Käßner et al. 2021). The zircons from sample Frau have the lowest $\delta^{18}O$ values compared to the above-mentioned Variscan igneous rocks but also compared to quartzo-feldspathic basement rocks from the Erzgebirge (grey and red gneisses). This points to either a higher melt temperature and/or a different source with lower $\delta^{18}O$ values like basic

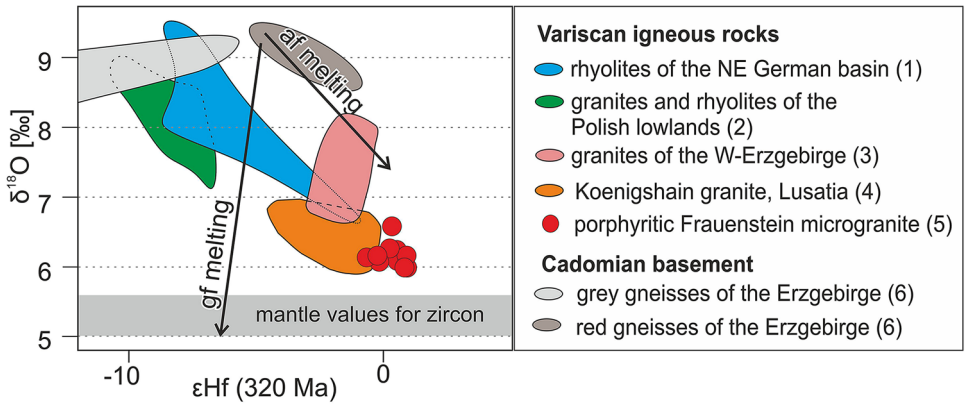

Fig. 8 εHf (320 Ma) versus $\delta^{18}O$ values from the same spot locations within zircons from sample Frau (Frauenstein microgranite ring dyke) in comparison with data from Variscan basement gneisses and granites/rhyolites of the Erzgebirge, NE German Basin, and Polish Lowlands. Data are from: 1: Pietranik et al. (2013), 2: Słodczyk et al. (2018), 3: Tichomirowa et al. (2019b), 4: Käßner et al. (2021), 5: this study, 6: Tichomirowa et al. (2018). Abbreviations: af-melting—amphibolite facies melting, gf-melting-granulite-facies melting according to Tichomirowa et al. (2018)

melts. However, the zircon $\delta^{18}O$ values from the Frauenstein microgranite ring dyke are still elevated compared to typical mantle values (Valley 2003: 5.3 ± 0.3‰). Tichomirowa et al. (2019b) argued that the relatively low $\delta^{18}O$ values of zircons from other Variscan plutonic rocks in the Western Erzgebirge exclude a dominant metapelitic source for these rocks because shales display typical values ≥ 14‰ (Bindeman et al. 2016). For the source of the Frauenstein microgranite ring dyke, the low $\delta^{18}O$ values indicate an absence or very low abundance of metapelites and shales as source rocks. Some of the quartzo-feldspathic basement rocks (red gneisses) produced small-scale in situ melts during amphibolite facies Variscan metamorphism that developed lower $\delta^{18}O$ values and higher epsilon Hf values (Fig. 8, "af melting" arrow). However, these metamorphic quartzo-feldspathic rocks still have higher $\delta^{18}O$ values (ca. 7‰) compared to those from the ring dyke (ca. 6‰). Therefore, in addition to these fertile metamorphic rocks another source with low $\delta^{18}O$ values is necessary to achieve the oxygen isotope composition of the ring dykes. Basic melts are the most probable second source for the Frauenstein microgranite. A mafic melt input supports the concept of de Silva and Gregg (2014) that requires recharge/s of the magma chamber to keep magma temperatures high enough and to prevent viscous magma death. Eventually, this magma recharge can promote roof uplift and final eruption of such crystal-rich magmas like the microgranite ring dyke. In detailed studies that compare zoning of feldspar phenocrysts in the Teplice rhyolite and the microgranite ring dyke, Müller and Seltmann (2002) and Müller et al. (2005) have shown that clear indications for an input of basic magma are found only in the latest stages of the Teplice rhyolite (stage "TR3c") as well as in the microgranite ring dyke. In the ring dyke, the second stage of microgranite intrusion is chemically less evolved compared to the first intrusion stage, again confirming an input of a basic melt (Müller and Seltmann 2002). In contrast, Casas-García et al. (2021) disprove a basic melt input for the Teplice rhyolite and the microgranite ring dyke mainly on the base of homogeneous Nd and Pb isotope fingerprints that "represent intermediate ranges between crustal and mantle components of the Cadomain and Lower Paleozoic basement".

The zircon Hf model ages of the microgranite ring dyke (Table 4: 1.2–1.1 Ga) agree with Nd model ages (T_{DM2}: 1.3–1.2 Ga) from many other rocks of the ATVC (Walther et al. 2016; Casas-García et al. 2021) and their homogeneous ε_{Nd}-values (-1.9 to -3.7; Casas-García et al. 2021). These Nd model ages are younger than those of Cadomian basement rocks from the Erzgebirge (Kröner et al. 1995; Tichomirowa et al. 2001; Mingram and Rötzler 1999: grey gneisses = 1.8–1.6 Ga, Ordovician red gneisses: 1.6–1.5 Ga). No Nd isotope data were published for Paleozoic sedimentary rocks (shale, arkose) from Saxothuringia of the Bohemian Massif. Cambro-Ordovician shales and pelites from other regions of the Variscan belt (Iberia, French Massif Central) have typical Nd model ages between 1.8 and 1.4 Ga (Nägler et al. 1995; Simien et al. 1999; Vila and Pin 2016) that are distinctly older compared to the analysed Variscan granites and rhyolites. Unfortunately, no Nd model ages were published for metamorphic melts in the Erzgebirge, but their zircon Hf model ages are 1.3–1.2 Ga (Tichomirowa et al. 2018). If metamorphic quartzo-feldspathic rocks were the major source of caldera-stage ATVC melts, then the slightly younger model ages require a minor input from a juvenile source (e.g. mantle melts). Indeed, old xenocrystic zircons (> 350 Ma) are scarce for these rocks and the very few xenocrystic ages between 323 and 341 Ma (Table 3) support the assumption that metamorphic quartzo-feldspathic

rocks could be the dominant source. In contrast, the earlier pre-caldera Flaje granite and SAC volcanics have higher abundances of xenocrystic pre-Variscan zircons (Hoffmann et al. 2013; Tomek et al. 2022; Table 3) pointing to another dominant source with a higher contribution of pre-Variscan basement rocks for their melts.

Conclusions

The obtained high-precision U–Pb zircon ages document a substantial time gap (7–8 Myr) between the pre-caldera Schönfeld-Altenberg Complex (SAC) and the main volcanic caldera stage of the ATVC. The volcanic rocks of the SAC represent the earliest volcanic activity in the Erzgebirge and central Europe at ca. 322 Ma, indicating a (sub)surface erosion level in the Southern Erzgebirge already at this time. According to the new high-precision zircon data, the Teplice rhyolite body formed during a relatively short time interval between 314 and 313 Ma. At the same time, the microgranite ring dyke as well as (at least) part of the rhyolitic dykes of the SBDS were formed. Accordingly, the new age data support the previously suggested close genetic and temporal relationship between the TR, the microgranite ring dyke, and the SBDS. The age of the ring dyke (314–313 Ma) can now be considered as the best estimate for the climactic stage of the ATVC, as the ring dyke is generally accepted as a syn-collapse intrusion.

Compared to Variscan igneous rocks of the northern part of the Eastern Erzgebirge, the SAC formed slightly earlier (ca. 322 Ma) than the deeply intruded Niederbobritzsch granite (320–318 Ma). Remarkably, the main magmatic activity leading to the formation of calderas in the ATVC and the Tharandt Forest was mainly contemporaneously (at ca. 314–312 Ma). These data document a large and long-standing upper crustal silicic magmatic system in the whole Eastern Erzgebirge stretching about 60 km along a NNW-SSE trending zone that is parallel to the Elbe Fault Zone. Possibly, the preceding Variscan metamorphism (ca. 340 Ma) as well as the pre-climactic plutons (Niederbobritzsch, Flaje: ca. 322–318 Ma) and volcanics (SAC: ca. 322 Ma) played an important role in a continuous increase of the upper crustal temperature and thereby affected the thermal and mechanical behaviours of the upper crustal host rocks as supposed as a necessary prerequisite for later voluminous and long-living magma systems (e.g. Folkes et al. 2011; de Silva and Gregg 2014).

We present the first zircon Hf-O-isotope data from the microgranite ring dyke of the ATVC. These data confirm the generally accepted crustal origin of the Variscan melts. However, the zircon Hf-O isotope ratios from the widespread occurring quartzo-feldspathic Cadomian basement rocks (gneisses) are too variable and too different to assume that these rocks could be the dominant source rocks. Consequently, preceding homogenization by melting is a prerequisite. The exceptional homogeneity of O isotopes can be interpreted as evidence for long-lasting convective stirring in the magma body. Smalls scale in situ melts during Variscan amphibolite-facies metamorphism produced fertile quartzo-feldspathic rocks with already pre-homogenized Hf-O isotope ratios and with model ages of about 1.2–1.1 Ga and are probably the dominant source of microgranite ring dyke melts. In addition, a second and more juvenile source (basic melts) is necessary to explain the low oxygen isotope ratios of the crystal-rich microgranite syn-climactic ring dyke.

Acknowledgements The authors are grateful to Filip Tomek and Reneė González Guzmán for their very helpful and constructive reviews. We thank the Saxon Geological Survey for financial support and the Isotope Research Centre in St. Petersburg (Russia) for SHRIMP measurements. The NordSIMS facility was supported by Swedish Research Council infrastructure grant 2017-00671 at the time of analysis; this is NordSIMS contribution 711.

Author contributions All authors contributed to the study conception and design. Material preparation, data collection, and analysis were performed by AK and MT. The first draft of the manuscript was written by MT and all authors commented on previous versions of the manuscript. All authors read and approved the final manuscript.

Funding Open Access funding enabled and organized by Projekt DEAL.

References

Benek R (1991) Aspects of volume calculation of paleovolcanic eruptive products: the example of the Teplice rhyolite (east Germany). Z Geol Wiss 19:379–389

Berger HJ, Felix M, Görne S, Koch E, Krentz O, Förster A, Förster HJ, Konietzky H, Lunow C, Walter K, Schulz H, Stanek K, Wagner S (2011) Tiefengeothermie Sachsen, 1. Arbeitsetappe 09/2009–07/2010. Schriftenreihe des LfULG Heft 9/2011, p 108

Bindeman IN, Valley JW (2002) Oxygen isotope study of the Long Valley magma system, California: isotope thermometry and convection in large silicic magma bodies. Contrib Miner Pet 144(2):185–205

Bindeman IN, Bekker A, Zakharov DO (2016) Oxygen isotope perspective on crustal evolution on early earth: a record of Precambrian

shales with emphasis on Paleoproterozoic glaciations and Great Oxygenation Event. Earth Planet Sci Lett 437:101–113
Black LP, Kamo SL, Allen CM, Aleinikoff JN, Davies DW, Korsch RJ, Foudoulis C (2003) TEMORA 1: a new zircon standard for Phanerozoic U-Pb geochronology. Chem Geol 200:155–170
Black LP, Kamo SL, Allen CM, Davis DW, Aleinikoff JN, Valley JW, Mundil R, Campbell IH, Korsch RJ, Williams IS, Foudoulis C (2004) Improved $^{206}Pb/^{238}U$ microprobe geochronology by the monitoring of a trace-element related matrix effect; SHRIMP, ID-TIMS, ELA-ICP-MS and oxygen isotope documentation for a series of zircon standards. Chem Geol 205:115–140
Bouvier A, Vervoort JD, Patchett PJ (2008) The Lu-Hf and Sm-Nd isotopic composition of CHUR: Constraints from unequilibrated chondrites and implications for the bulk composition of terrestrial planets. Earth Planet Sci Lett 273:48–57
Bowring JF, McLean NM, Bowring SA (2011) Engineering cyber infrastructure for U-Pb geochronology: tripoli and U-Pb_Redux. Geochem Geophys Geosyst 12(6):19
Breiter K (2012) Nearly contemporaneous evolution of the A- and S-type fractionated granites in the Krušné hory/Erzgebirge Mts, Central Europe. Lithos 151:105–121
Breiter K, Förster HJ, Seltmann R (1999) Variscan silicic magmatism and related tin-tungsten mineralization in the Erzgebirge-Slavkovsky les metallogenic province. Miner Depos 34:505–521
Breiter K, Novák JK, Chlupáčová M (2001) Chemical evolution of volcanic rocks in the Altenberg-Teplice Caldera (Eastern Krušne Hory Mts., Czech Republic, Germany). 6th International Mineralogical-Petrological Symposium, Magurka, August 29–31, 2000. Geolines 13:17–22
Breiter K, Svojtka M, Ackerman L, Švecova K (2012) Trace element composition of quartz from the Variscan Altenberg-Teplice caldera (Krušné hory/Erzgebirge Mts, Czech Republic/Germany): Insights into the volcano-plutonic complex evolution. Chem Geol 326–327:38–50
Breitkreuz C, Lapp M, Käßner A, Tichomirowa M, Lapp M, Huang S, Stanek K (2021) The Late Carboniferous deeply eroded Tharandt Forest Caldera-Niederbobritzsch Granite Complex: A post-Variscan long-standing magmatic system in central Europe. Int J Earth Sci 110:1265–1292. https://doi.org/10.1007/s00531-021-02015-x
Casas-García R, Rapprich V, Breitkreuz C, Svojtkac M, Lapp M, Stanek K, Hofmann M, Linnemann U (2019) Lithofacies architecture, composition, and age of the Carboniferous Teplice Rhyolite (German–Czech border): Insights into the evolution of the Altenberg-Teplice Caldera. J Volcanol Geotherm Res 386:106662. https://doi.org/10.1016/j.jvolgeores.2019.106662
Casas-García R, Rapprich V, Repstock A, Magna T, Schulz B, Kochergina YVE, Breitkreuz C (2021) Crustal vs. mantle contributions in the Erzgebirge/Krušne hory Mts. magmatism: Implications for generation of zoned, A-type silicic rocks in the late-Variscan Altenberg-Teplice Caldera, Central Europe. Lithos. https://doi.org/10.1016/j.lithos.2021.106429
Chen RX, Zheng YF (2017) Metamorphic zirconology of continental subduction zones. J Asian Earth Sci 145:149–176
Christiansen RL (2001) The quaternary and Pliocene Yellowstone Plateau Volcanic Field of Wyoming, Idaho, and Montana. U. S. Geol. Surv. Prof. Pap. 729-G, p 145
Condon DJ, Schoene B, McLean NM, Bowring SA, Parrish RR (2015) Metrology and traceability of U-Pb isotope dilution geochronology (EARTHTIME Tracer Calibration Part I). Geochim Cosmochim Acta 164:464–480
Conrad W, Haupt M, Bolsche J (1994) Interpretation des tiefenseismischen Regionalprofils EV01-EV02/1978-80 Vogtland-Erzgebirge-Lausitz (Adorf – Gutzen) mit Hilfe von Gravimetrie und Magnetik. Z Geol Wiss 22:603–615
de Silva SL, Gregg PM (2014) Thermomechanical feedbacks in magmatic systems: Implications for growth, longevity, and evolution of large caldera-forming magma reservoirs and their supereruptions. J Volcanol Geotherm Res 282:77–91
Edel JB, Schulmann K, Lexa O, Lardeaux JM (2018) Late Palaeozoic palaeomagnetic and tectonic constraints for amalgamation of Pangea supercontinent in the European Variscan Belt. Earth Sci Rev 177:589–612
Folkes CB, Wright HM, Cas RAF, de Silva SL, Lesti C, Viramonte JG (2011) A re-appraisal of the stratigraphy and volcanology of the Cerro Galan volcanic system, NW Argentina. Bull Volcanol 73(10):1427–1454. https://doi.org/10.1007/s00445-011-0459-y
Förster HJ, Romer RL (2010) Carboniferous magmatism. In: Linnemann U, Romer RL (eds) Pre-Mesozoic geology of Saxo-Thuringia. Schweizerbart Science Publishers, Stuttgart, pp 287–310
Förster HJ, Tischendorf G, Trumbull RB, Gottesmann B (1999) Late-collisional granites in the Variscan Erzgebirge, Germany. J Pet 40(11):1613–1645
Gerdes A, Zeh A (2006) Combined U-Pb and Hf isotope LA-(MC)ICP-MS analyses of detrital zircons: comparison with SHRIMP and new constraints for the provenance and age of an Armorican metasediment in Central Germany. Earth Planet Sci Lett 249:47–61
Gerstenberger H, Haase G (1997) A highly effective emitter substance for mass spectrometric Pb isotope ratio determinations. Chem Geol 136:309–312
Glazner AF (2021) Thermal constraints on the longevity, depth, and vertical extent of magmatic systems. Geochem Geophys Geosyst 22(4):e2020GC009459
Heinonen A, Anderson T, Rämö T, Whitehouse M (2015) The source of Proterozoic anorthosite and rapakivi granite magmatism: evidence from combined in situ Hf-O isotopes of zircon in the Ahvenisto complex, southeastern Finland. J Geol Soc 172:103–112
Hoffmann U, Breitkreuz C, Breiter K, Sergeev S, Stanek K, Tichomirowa M (2013) Carboniferous-Permian volcanic evolution in Central Europe–U/Pb ages of volcanic rocks in Saxony (Germany) and northern Bohemia (Czech Republic). Int J Earth Sci 102:73–99
Horstwood MSA, Košler J, Gehrels G, Jackson SE, McLean NM, Paton C, Pearson NJ, Sircombe K, Sylevester P, Vermeesch P, Bowring JF, Condon DJ, Schoene B (2016) Community-derived standards for LA-ICP-MS U-(Th-)Pb geochronology: uncertainty propagation, age interpretation and data reporting. Geostand Geoanal Res 40(3):311–332
Hoth K, Wasternack J, Berger HJ, Breiter K, Mločoch B, Schovánek P (1995) Geologische Karte Erzgebirge / Vogtland, 2nd edn. Sächsisches Landesamt für Umwelt und Geologie, Bereich Boden und Geologie, Freiberg
Jaffey AH, Flynn KF, Glendenin LE, Bentley WC, Essling AM (1971) Precision measurement of half-lives and specific activities of 235U and 238U. Phys Rev C. https://doi.org/10.1103/PhysRevC.4.1889
Käßner A, Tichomirowa M, Lapp M, Leonhardt D, Whitehouse M, Gerdes A (2021) Two-phase late Paleozoic magmatism (~ 313–312 and ~ 299–298 Ma) in the Lusatian Block and its relation to large scale NW striking fault zones: evidence from zircon U-Pb CA–ID–TIMS geochronology, bulk rock- and zircon chemistry. Int J Earth Sci. https://doi.org/10.1007/s00531-021-02092-y
Kempe U, Wolf D, Ebermann U, Bombach K (1999) 330 Ma Pb/Pb single zircon evaporation ages for the Altenberg Granite Porphyry, Eastern Erzgebirge (Germany): implications for Hercynian granite magmatism and tin mineralisation. Z Geol Wiss 27:358–400
Kröner A, Willner AP (1998) Time of formation and peak of Variscan HP-HT metamorphism of quartz-feldspar rocks in the central Erzgebirge, Saxony, Germany. Contrib Miner Pet 132:1–20
Kröner A, Willner AP, Hegner E, Frischbutter A, Hofmann J, Bergner R (1995) Latest Precambrian (Cadomian) zircon ages, Nd

isotopic systematics and p-T evolution of granitoid orthogneisses of the Erzgebirge, Saxony and Czech Republic. Geol Rundsch 84:437–456

Kroner U, Görz I (2010) Variscan assemblage of the allochthonous domain of the Saxo-Thuringian Zone - a tectonic model. In: Linnemann U, Romer RL (eds) Pre-Mesozoic geology of Saxo-Thuringia. Schweizerbart Science Publishers, Stuttgart, pp 271–286

Kryza R, Schaltegger U, Oberc-Dziedzic T, Rin C, Ovtcharova M (2014) Geochronology of a composite granitoid pluton: a high-precision ID-TIMS U-Pb zircon study of the Variscan Karkonosze Granite (SW Poland). Int J Earth Sci 103:683–696

Lobin M (1986) Aufbau und Entwicklung des Permosiles im östlichen und mittleren Erzgebirge [Ph.D. thesis]. Bergakademie, Freiberg

Ludwig K (2000) SQUID 100, a user's manual. Berkeley Geochronology Center Special Publication, Berkeley

Lützner H, Tichomirowa M, Käßner A, Gaupp R (2021) Latest Carboniferous to early Permian volcano-stratigraphic evolution in Central Europe – U-Pb CA-ID-TIMS ages of volcanic rocks in the Thuringian Forest Basin (Germany). Int J Earth Sci 110:377–398

Massonne HJ (2003) A comparison of evolution of diamondiferous quartz-rich rocks from the Saxonian Erzgebirge and the Kokchetav Massif: Are so-called diamondiferous gneisses magmatic rocks? Earth Planet Sci Lett 216:347–364

Mattinson JM (2005) Zircon U-Pb chemical abrasion ("CA-TIMS") method: combines annealing and multi-Step partial dissolution analysis for improved precision and accuracy of zircon ages. Chem Geol 220:47–66

Miller J, Matzel J, Miller C, Burgess S, Miller R (2007) Zircon growth and recycling during the assembly of large, composite arc plutons. J Volcanol Geotherm Res 167:282–299

Mingram B, Rötzler K (1999) Geochemische, petrologische und geochronologische Untersuchungen im Erzgebirgskristallin - Rekonstruktion des Krustenstapels. Schr Geol Wiss 9:80

Mlčoch B, Skácelová Z (2010) Geometry of the Altenberg-Teplice Caldera revealed by the borehole and seismic data in its Czech part. J Geosci 55:217–229

Moesta G (1928) Brüche und Porphyreffusionen im östlichen Erzgebirge. Z Dtsch Geol Gesell 80:343–408

Müller A, Seltmann R (2002) Plagioclase-mantled K-feldspar in the Carboniferous porphyritic microgranite of Altenberg-Frauenstein, Eastern Erzgebirge/Krušne Hory. Bull Geol Soc Fin 74:53–78

Müller A, Breiter K, Seltmann R, Pécskay Z (2005) Quartz and feldspar zoning in the eastern Erzgebirge volcano-plutonic complex (Germany, Czech Republic): Evidence of multiple magma mixing. Lithos 80:201–227

Müller A, Thomas R, Wiedenbeck M, Seltmann R, Breiter K (2006) Water content of granitic melts from Cornwall and Erzgebirge: a Raman spectroscopy study of melt inclusions. Eur J Miner 18:429–440

Müller A, Seltmann R, Kober B, Eklund O, Jeffries T, Kronz A (2008) Compositional zoning of rapakivi feldspars and coexisting quartz phenocrysts. Can Miner 46:1417–1442

Nägler TF, Schäfer HJ, Gebauer D (1995) Evolution of the Western European continental crust: implications from Nd and Pb isotopes in Iberian sediments. Chem Geol 121:345–357

Opluštil S, Schmitz M, Cleal CJ, Martínek K (2016) A review of the Middle-Late Pennsylvanian west European regional substages and floral biozones, and their correlation to the Geological Time Scale based on new U-Pb ages. Earth Sci Rev 154:301–335

Pietranik A, Storey C, Kierczak J (2013) The Niemcza diorites and monzodiorites (Sudetes, SW Poland): a record of changing geotectonic setting at ca. 340 Ma. Geol Q 57:325–334

Romer RL, Thomas R, Stein HJ, Rhede D (2007) Dating multiple overprinted Sn-mineralized granites – examples from the Erzgebirge, Germany. Miner Depos 42:337–359

Romer RL, Förster HJ, Štemprok M (2010) Age constraints for the late-Variscan magmatism in the Altenberg-Teplice Caldera (Eastern Erzgebirge/Krušné hory). N Jahrb Miner (abh) 187:289–305

Rötzler K, Schumacher R, Maresch WV, Willner AP (1998) Characterization and geodynamic implications of contrasting metamorphic evolution in juxtaposed high-pressure units of the Western Erzgebirge (Saxony, Germany). Europ J Miner 10:261–280

Schaltegger U, Schmitt AK, Horstwood MSA (2015) U-Th–Pb zircon geochronology by ID-TIMS, SIMS, and laser ablation ICP-MS: Recipes, interpretations, and opportunities. Chem Geol 402:89–110

Schmädicke E (1991) Quartz pseudomorphs after coesite in eclogites from the Saxonian Erzgebirge. Eur J Miner 3:231–238

Schmädicke E, Mezger K, Cosca MA, Okrusch M (1995) Variscan Sm-Nd and Ar-Ar ages of eclogite facies rocks from the Erzgebirge, Bohemian Massif. J Metamorp Geol 13(5):537–552

Schmädicke E, Will TM, Ling X, Li XH, Li QL (2018) Rare peak and ubiquitous post-peak zircon in eclogite: Constraints for the timing of UHP and HP metamorphism in Erzgebirge, Germany. Lithos 322:250–267

Schoene B, Crowley JL, Condon DC, Schmitz MD, Bowring SA (2006) Reassessing the uranium decay constants for geochronology using ID-TIMS U-Pb data. Geochim Cosmochim Acta 70:426–445

Schulmann K, Konopásek J, Janoušek V, Lexa O, Lardeaux JM, Edel JB, Štipská US (2009) An Andean type Paleozoic convergence in the Bohemain Massif. Comptes Rendus Geosci 314:266–286

Schulmann K, Lexa O, Janoušek V, Lardeaux JM, Edel JB (2014) Anatomy of a diffuse cryptic suture zone: An example from the Bohemian Massif, European Variscides. Geol 42:275–278

Schust F (1980) Zum Zusammenhang zwischen der paläogeographischen Entwicklung und der Intrusionstiefe der Granite im Osterzgebirge. Z Angew Geol 26:405–411

Sebastian U (2013) Die Geologie des Erzgebirges. Springer Spektrum, Berlin, p 268

von Seckendorff V (2012) Der Magmatismus in und zwischen den spätvariscischen permokarbonen Sedimentbecken in Deutschland. In: Deutsche Stratigraphische Kommission (Hrsg, Koordination und Redaktion: Lützner H, Kowalczyk G für die Subkommission Perm-Trias): Stratigraphie von Deutschland X. Rotliegend. Teil I: Innervariscische Becken. Schriftenr Dt Ges Geowiss 61:743–860

Seifert T (2008) Metallogeny and petrogenesis of lamprophyres in the Mid-European Variscides. Millpress Science Publications, Rotterdam, p 304

Seltmann R, Schilka W (1995) Late Variscan crustal evolution in the Altenberg-Teplice caldera. Evidence from new geochemical and geochronological data. Terra Nostra 98:120–212

Simien F, Mattauer M, Allegre CJ (1999) Nd isotopes in the stratigraphical record of the Montagne Noire (French Massif Central): no significant Palaeozoic juvenile inputs, and pre-Hercynian paleogeography. J Geol 107:87–97

Sláma J, Košler J, Condon DJ, Crowley JL, Gerdes A, Hanchar JM, Horstwood MSA, Morris GA, Nasdala L, Norberg N, Schaltegger U, Schoene B, Tubrett N, Whitehouse MJ (2008) Plesovice zircon: a new natural reference material for U-Pb and Hf isotopic microanalysis. Chem Geol 249:1–35

Słodczyk E, Pietranik A, Glynn S, Wiedenbeck M, Breitkreuz C, Dhuime B (2018) Contrasting sources of Late Paleozoic rhyolite magma in the Polish Lowlands: evidence from U-Pb ages and Hf and O isotope composition in zircon. Int J Earth Sci 107:2065–2081

Stacey JC, Kramers JD (1975) Approximation of terrestrial lead isotope evolution by a two-stage model. Earth Planet Sci Lett 26:207–221

Štemprok M (2016) Drill hole CS-1 penetrating the Cínovec/Zinnwald granite cupola (Czech Republic): an A-type granite with important hydrothermal mineralization. J Geosc 61:395–423

Štemprok M, Holub FV, Novak JK (2003) Multiple magmatic pulses of the Eastern Volcano-Plutonic Complex, Krušné hory/Erzgebirge batholith, and their phosphorus contents. Bull Geosci 78:277–296

Thomas R (1992) Results of investigations on melt inclusions in various magmatic rocks from the northern border of the Bohemian Massif. In: Kukal Z (ed) Proceedings of the 1st international conference on the Bohemian Massif. Czech Geological Survey, Prague, pp 298–306

Tichomirowa M, Köhler R (2013) Discrimination of protolithic versus metamorphic zircon ages in eclogites: Constraints from the Erzgebirge metamorphic core complex (Germany). Lithos 177:436–450

Tichomirowa M, Berger HJ, Koch EA, Belyatski B, Götze J, Kempe U, Nasdala L, Schaltegger U (2001) Zircon ages of high-grade gneisses in the Eastern Erzgebirge (Central European Variscides) – constraints on origin of the rocks and Precambrian to Ordovician magmatic events in the Variscan foldbelt. Lithos 56:303–332

Tichomirowa M, Whitehouse MJ, Nasdala L (2005) Resorption, growth, solid state recrystallisation, and annealing of granulite facies zircon - a case study from the Central Erzgebirge, Bohemian Massif. Lithos 82:25–50

Tichomirowa M, Whitehouse M, Gerdes A, Schulz B (2018) Zircon (Hf, O isotopes) as melt indicator: Melt infiltration and abundant new zircon growth within melt rich layers of granulite-facies lenses versus solid-state recrystallization in hosting amphibolite-facies gneisses (central Erzgebirge, Bohemian Massif). Lithos 302–303:65–68. https://doi.org/10.1016/j.lithos.2017.12.020

Tichomirowa M, Käßner A, Sperner B, Lapp M, Leonhardt D, Linnemann U, Münker C, Ovtcharova M, Pfänder JA, Schaltegger U, Sergeev S, von Quadt A (2019a) Dating multiply overprinted granites: the effect of protracted magmatism and fluid flow on dating systems (zircon U-Pb: SHRIMP/SIMS, LA-ICP-MS, CA-ID-TIMS; and Rb-Sr, Ar-Ar) – granites from the Western Erzgebirge (Bohemian Massif, Germany). Chem Geol 519:11–38

Tichomirowa M, Gerdes A, Lapp M, Leonhardt D, Whitehouse M (2019b) The Chemical Evolution from Older (323–318 Ma) towards Younger highly evolved tin granites (315–314 Ma) – sources and metal enrichment in Variscan granites of the western Erzgebigre (Central European Variscides, Germany). Minerals 9:1–30

Tischendorf G (1989) Silicic magmatism and metallogenesis of the Erzgebirge. Central Institute for Physics of the Earth, Postdam, p 316

Tomek F, Žák J, Svojtka M, Finger F, Waitzinger M (2018) Emplacement dynamics of syn-collapse ring dikes: an example from the Altenberg-Teplice caldera Bohemian Massif. Geol Soc Am Bull. https://doi.org/10.1130/B35019.1

Tomek F, Žák J, Svojtka M, Finger F, Waitzinger M (2019) Emplacement dynamics of syn-collapse ring dikes: An example from the Altenberg-Teplice caldera, Bohemian Massif. Geol Soc Am Bull 131:997–1016

Tomek F, Opluštil S, Svojtka M, Špillar V, Rapprich V, Míková J (2022) Altenberg-Teplice Caldera sourced Westphalian fall tuffs in the central and western Bohemian Carboniferous basins (eastern Variscan belt). Int Geol Rev 64:441–468. https://doi.org/10.1080/00206814.2020.1858357

Valley JW (2003) Oxygen isotopes in zircon. Rev Miner Geochem 53:343–385

Vervoort JD, Blichert-Toft J (1999) Evolution of the depleted mantle: Hf isotope evidence from juvenile rocks through time. Geochim Cosmochim Acta 63:533–556

Vila M, Pin C (2016) Geochemistry and Nd isotope signature of the Collserola Range Palaeozoic succesion (NE Iberia): Gondwana heritage and pre-Mesozoic geodynamic evolution. Geol Mag 153:643–662

Walther D, Breitkreuz C, Rapprich V, Kochergina Y, Chlupáčová M, Lapp M, Stanek K, Magna T (2016) The Late Carboniferous Schönfeld-Altenberg Depression on the NW margin of the Bohemian Massif (Germany/ Czech Republic): volcanosedimentary and magmatic evolution. J Geoscience 61:371–393

Wetzel HU (1984) Spätvariszische Bruchtektonik und subsequente Gangmagmatite als Ausdruck der Krustenentwicklung im Osterzgebirge (Altenberger Scholle). Zentralinst. f. Physik d. Erde, Potsdam, Akad. d. Wiss. d. DDR, Potsdam unpubl PhD, p 364 (in German)

Widmann P, Davies JHFL, Schaltegger U (2019) Calibrating chemical abrasion: its effects on zircon crystal structure, chemical composition and U-Pb age. Chem Geol 511:1–10

Wiedenbeck M, Alle P, Corfu F, Griffin WL, Meier M, Oberli F, von Quadt A, Roddick JC, Spiegel W (1995) Three natural zircon standards for U – Th – Pb, Lu – Hf, trace element and REE analysis. Geostand Newsl 19:1–23

Wiedenbeck M, Hanchar J, Peck WH, Sylvester P, Valley J, Whitehouse M, Kronz A, Morishita Y, Nasdala L (2004) Further characterization of the 91500 zircon crystal. Geostand Geoanal Res 28:9–39

Williams IS (1998) U-Th-Pb geochronology by ion microprobe. Rev Econ Geol 7:1–35

Willner AP, Rötzler K, Maresch WV (1997) Pressure-Temperature and fluid evolution of quartzo-feldspathic metamorphic rocks with a relic high-pressure, granulite-facies history from the Central Erzgebirge (Saxony, Germany). J Pet 38:307–336

Winter C, Breitkreuz C, Lapp M (2008) Textural analysis of a Late Palaeozoic coherent to pyroclastic rhyolitic dyke system near Burkersdorf (Erzgebirge, Saxony, Germany). Geol Soc Lond Spec Publ 302:197–219